Electronic band structure of high-symmetry homobilayers of transition metal dichalcogenides

Electronic band structure of high-symmetry homobilayers of transition metal dichalcogenides

Heng Zhang,[1,2] Wen Xu,[1,3,4,*] Yiming Xiao,[4]
Francois M. Peeters,[5,6] and Milorad V. Milošević[6,†]

[1]*Key Laboratory of Materials Physics,*
Institute of Solid State Physics, HFIPS,
Chinese Academy of Sciences, Hefei 230031, China
[2]*University of Science and Technology of China, Hefei 230026, China*
[3]*Micro Optical Instruments Inc., Shenzhen 518118, China*
[4]*School of Physics and Astronomy and Yunnan Key Laboratory of Quantum Information,*
Yunnan University, Kunming 650091, China
[5]*Micro Optical Instruments Inc., 518118 Shenzhen, China*
[6]*Department of Physics, University of Antwerp,*
Groenenborgerlaan 171, B-2020 Antwerp, Belgium

(Dated: October 15, 2024)

Abstract

High-symmetric homobilayer transition metal dichalcogenides (TMDs) are important members of the bilayer (BL) van der Waals material family. Here we present a systematic study of the electronic band structure in low-energy regime in homo-BL TMD structures by using the standard $k \cdot p$ method. Six types of BL TMD stacking configurations, which satisfy the C_3 symmetry are considered and they are H_M^M, H_X^M, H_X^X, R_M^M, R_X^M, and R_M^X. The intrinsic spin-orbit coupling (SOC) in the conduction and valence bands and the phase of interlayer hopping matrix elements are included in our investigation. Taking BL MoS_2 as an example, we examine the electronic energy spectra, the electron density of states, and the Fermi energies in these BL structures. We find that the electron energy dispersions in high-symmetric BL TMDs are not parabolic-like, where the band parameters (such as the energy gap, the effective electron band mass and the fourth-order correction coefficient in different subbands) depend markedly on the stacking configurations. Interestingly, the spin splitting in H-stacked BL TMDs is suppressed because of center-inversion symmetry and time-reversal symmetry. Importantly, the phase of the interlayer hopping matrix element affects significantly the electronic properties of H_X^X and R_M^M stacked BL TMDs. The methodology and the results presented in this study can foster further exploration of the basic physical properties of BL TMDs for potential applications in electronics and optoelectronics.

PACS numbers:

*Electronic address: wenxu_issp@aliyun.com

†Electronic address: milorad.milosevic@uantwerpen.be

I. INTRODUCTION

Since the discovery of graphene [1], the fabrication and investigation of atomically thin two-dimensional (2D) electronic systems (2DESs) have quickly become the main focusing point in scientific research due to their potential applications in next-generation nanoelectronic and optoelectronic devices [2–4]. In particular, monolayer (ML) transition metal dichalcogenides (TMDs) have attracted immense attention for both experimental and theoretical investigations because of their novel electronic and optical properties [5–10], which can be utilized for the realization of the spintronic and valleytronic devices to be applied in, e.g., information technology [7, 11]. Moreover, since the discovery of superconductivity in twisted bilayer (BL) graphene [12], the investigation of BL-based 2DESs has become a hot and fast-growing field of research in condensed matter physics, electronics and optoelectronics [11, 13, 14]. In a BL 2DES, the interactions between two layers with specific stacking order can significantly modify the physical properties of the electronic system [6, 7, 15, 16] and, thus, provide one more freedom for the modification and control of the corresponding electronic devices.

In recent years, BL TMD systems have been realized via, e.g, fabricating two ML TMDs bonded by the van der Waals (vdW) force [6, 17]. Therefore, the twistronic features of the BL systems can be observed by tuning the vdW heterostructure from normal to the inverted type-II regime through, e.g., taking different stacking orders (i.e., tuning the interlayer coupling) and/or applying an interlayer bias voltage [18]. The BL TMD structures have demonstrated a lot of interesting and important physical properties such as spin, valley, and orbital Hall effects [19–21], Nernst effect [22], magneto electric effect [23], spin-layer locking effect [24], etc. They have been considered as advanced materials not only in spintronics and valleytronics but also in twistronics. It is known that both translation and twisting of two TMD MLs are practical and feasible approaches to prepare and define the microscopic structure of a BL 2DES [25]. To date, the major research attention has been focused on the physical properties of BL TMDs as a consequence of sliding or twist of two TMD MLs in order to achieve the topological mosaics in moiré superlattices [13]. From a viewpoint of condensed matter physics, the translation of two TMD layers can also result in high-symmetric BL electronic configurations. For example, two same or homogenous TMD MLs can form the basic $2H$ or $3R$ stacking order, which can be exfoliated from the bulk phases of

TMD materials [26, 27]. By translating a ML with $2H$ or $3R$ stacking order, one can achieve the other high-symmetric stacking configurations in homo-BL TMDs. Up to now, most of the research has been focused on the $2H$ and $3R$ stacking BL TMD structures [6, 26–28]. For the application of BL TMDs as advanced electronic and optoelectronic materials, it is of great significance to examine the basic electronic properties of BL TMDs with other high-symmetric lattice structures. This becomes the prime motivation of this study.

Electronic band structure is the central feature of physics to describe an electronic material. At present, the theoretical studies of the electronic band structure of BL TMD systems have been mainly conducted using *ab initio* calculations [6], which is a numerical and CPU consuming approach. The tight-binding (TB) model has also been applied to calculate the electronic band structures of ML and BL TMD structures [10, 29, 30], which, however, is also nontrivial to obtain the analytical solutions when dealing with the BL TMD systems. It is known that $k\cdot p$ method can provide simple, transparent, and insightful solutions to the band structure of an electronic material in low electronic energy regime [31]. This can benefit greatly the further calculations of, e.g., the electronic transport and optical coefficients of the material. Normally, the electron Hamiltonian of a high-symmetric BL TMD system can be simplified as a 4×4 matrix using the $k\cdot p$ approach [32], which is easy to solve and to get the general analytical solutions of the electronic energy spectrum and wavefunctions. This approach has been successfully applied to study the electronic transport coefficients [33], orbital Hall effect [21], and magneto-optical properties [34] of $2H$ BL TMDs. The basic $k\cdot p$ Hamiltonian for high-symmetric BL TMDs has been proposed and examined by Tong *et al.* [32] in 2017 through introducing the interlayer hopping matrix elements. The theoretical principle and approach to derive the hopping matrix elements according to the symmetry of the stacking configuration in homogenous BL (or homo-BL) TMDs have also been developed [35, 36]. These published studies have established the basis for studying the electronic band structures in BL TMD systems. However, there is a lack in studying the electronic band structure in all six types of high symmetric homo-BL TMDs more systematically and comprehensively. In this study, we attempt to fill in this gap so that one can compare the features of these band structures not only qualitatively but also quantitatively. It should be pointed out that in previous studies, the elements of the interlayer hopping matrix in high-symmetric BL TMDs were taken as the real values in the $k\cdot p$ calculations. The effect of the phase angle during the interlayer hopping has often been ignored. The phase and phase

change during the electronic transition and interaction are important characteristics for a quantum system. For example, the discovery of the Ising superconductivity in gated MoS_2 in 2015 [37] indicates that the in-plane mirror symmetry can be broken in both ML and BL TMDs. Thus, the phase angles in the allowed hopping matrix elements in high-symmetric BL TMDs may not be zero. It is therefore necessary to examine the influence of the phase angle of the interlayer hopping matrix elements on the electronic band structure of high-symmetric BL TMDs, which is another important aspect of our present study. Furthermore, it would be significant and important to evaluate the band parameters of high-symmetric homo-BL TMDs, such as the energy gap in the BL system, the effective electron mass and the nonparabolicity in different subbands. These parameters are normally experimentally measurable and have not yet been examined specifically.

In this paper, we conduct a detailed theoretical investigation of the electronic band structure in six types of high-symmetric homo-BL TMD systems. The paper is organized as follows. The theoretical approaches for the calculations of the electronic energy spectra and wavefunctions, the BL band gap, the effective band masses, the high-order correction parameters of the energy spectra, the electronic density-of-states (DoS), and the Fermi energy for BL TMDs are developed in Sec. II. The numerical results of these properties for six types of high-symmetric BL MoS_2 are presented and discussed in Sec. III. The concluding remarks stemming from this study are summarized in Sec. IV.

II. THEORETICAL FRAMEWORK

A. Bi-layer stacking configurations

The $k \cdot p$ Hamiltonian used in this study for BL TMDs is constructed on the basis of the Hamiltonian for ML TMDs. It is known that the ML TMDs, such as MX_2 with M = Mo or W and X = S or Se, is a hexagonal crystal in which the metal atom (M) is sandwiched between the chalcogen atoms (X) on both sides. In this study, we consider that the homo-BL TMD structures with six types of high-symmetric stacking orders are realized by two ML TMDs. They are H^M_M, H^M_X, or $2H$, H^X_X, R^M_M, R^M_X, and R^X_M structures. These stacking configurations satisfy the C_3 symmetry and their crystal structures are shown in Fig. 1.

B. Electron Hamiltonian

It is known from the results obtained from, e.g., the *ab initio* calculations [6] that the conduction and valence band edges near K and $K^{'}$ points in ML TMDs are attributed mainly to d_{z^2}, d_{xy}, and $d_{x^2-y^2}$ orbits of the metal atoms. Namely, the electron wave functions are mainly based on $\psi_c = |d_{z^2}\rangle$ and $\psi_v^\tau = (|d_{x^2-y^2}\rangle + i\tau|d_{xy}\rangle)/\sqrt{2}$, with $\tau = \pm$ denoting the K or $K^{'}$ valley. Thus, we can utilize the electron Hamiltonian for ML TMDs to construct that for the BL TMD systems [23, 32–34, 38]. In this study, we consider a two-layer system with the same TMD material, i.e., the homo-BL TMD system. A minimal band model for this kind of BL structure in the neighborhood of the K/K$^{'}$ points in the band structure can be constructed by adding the interlayer hopping to the $k \cdot p$ model of the ML TMDs [5]. As a result, the single electron Hamiltonian for a homo-BL TMD system is composed of three basic parts, i.e.,

$$H = H_0 + H_{SOC} + H_{hopping}, \tag{1}$$

where H_0 stems from orbital interaction, H_{SOC} is induced by intrinsic spin-orbit coupling (SOC), and $H_{hopping}$ is attributed from interlayer hopping. Here we have neglected the effects

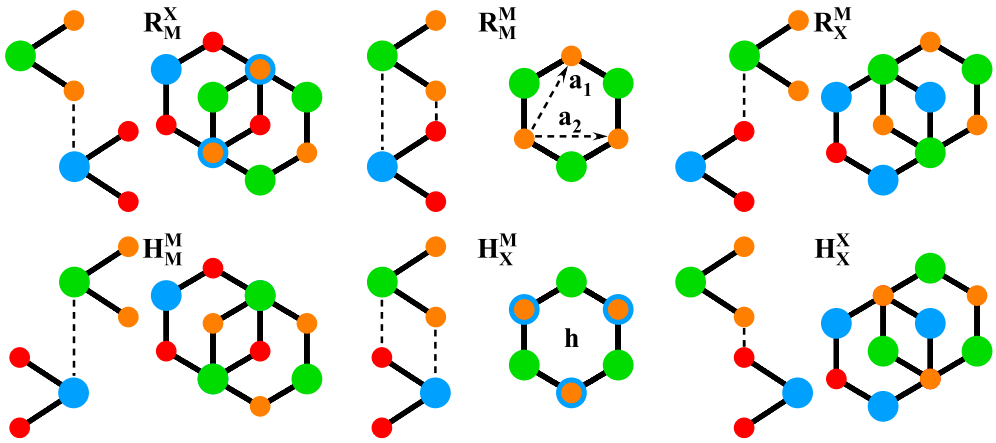

FIG. 1: Diagrammatic crystal structures of six types of high-symmetric homo-BL TMDs. Here, the big green/blue dots denote the metal atom (M) in upper/lower layer, the small orange/red dots denote the chalcogen atom (X) in upper/lower layer, and h marks the hexagon center. The dashed lines between atoms are perpendicular to the plane. $\mathbf{a}_1$ and $\mathbf{a}_2$ are the basic vectors of ML TMDs with $|\mathbf{a}_1| = |\mathbf{a}_2|$.

of the Rashba SOC and the proximity-induced exchange interaction in ML TMDs [39]. The electron Hamiltonian for a homo-BL TMD structure can be written as a 4×4 matrix

$$H(\mathbf{k}) = \begin{pmatrix} \Delta/2 + \epsilon\tau s\lambda_c & Ak^-_{\epsilon\tau} & t_{cc} & t_{cv} \\ Ak^+_{\epsilon\tau} & -\Delta/2 + \epsilon\tau s\lambda_v & t_{vc} & t_{vv} \\ t^*_{cc} & t^*_{vc} & \Delta/2 + \tau s\lambda_c & Ak^-_{\tau} \\ t^*_{cv} & t^*_{vv} & Ak^+_{\tau} & -\Delta/2 + \tau s\lambda_v \end{pmatrix}. \tag{2}$$

Here, $\mathbf{k} = (k_x, k_y)$ is the relative electron wavevector with respect to the K/K$'$ points, Δ is the band gap of ML TMDs, $A = at$ with a being the lattice constant of the ML TMD crystal and t the nearest-neighbor intralayer hopping coefficient, λ_c (λ_v) is the strength of intrinsic SOC in conduction (valence) band in ML TMDs, $s = \pm$ denotes to spin-up or down state (which is a good quantum number), $k^{\pm}_{\tau} = \tau k_x \pm ik_y$ with $\tau = \pm 1$ being the valley index, $k^{\pm}_{\epsilon\tau} = \tau k_x \pm i\epsilon k_y$ with $\epsilon = -1$ for H-stacking orders ($\mathrm{H^M_M}$, $\mathrm{H^M_X}$, and $\mathrm{H^X_X}$) and $\epsilon = +1$ for R-stacking orders ($\mathrm{R^M_M}$, $\mathrm{R^M_X}$, and $\mathrm{R^X_M}$) [32], $t_{\mu\mu'} = |t_{\mu\mu'}|e^{i\tau\phi_{\mu\mu'}}$ is the element of the interlayer hopping matrix with $\mu = (c, v)$ being an index regarding conduction or valence band, and $\phi_{\mu\mu'}$ is the phase angle of the interlayer hopping matrix element.

C. Electronic band structure

The Schrödinger equation for an electron with the Hamiltonian given by Eq. (2) can be solved analytically. At the fixed ϵ, τ, and s, the four eigenvalues in six types of high-symmetric BL TMD are the solutions of the equation

$$E^4 + b_3E^3 + b_2E^2 + b_1E + b_0 = 0, \tag{3}$$

where $E = E^{\gamma}_{\mu\nu}(\mathbf{k})$ with $\gamma = \tau s = \pm$. Four different solutions of Eq. (3) with the same ϵ and γ correspond to four eigenenergies, two of them belong to the conduction band ($\mu = c$) and the other two belong to the valence band ($\mu = v$). We find that it is convenient to introduce an index $\nu = (1, 2)$ to distinguish the higher/lower eigenenergy in conduction/valence band, i.e. $E^{\gamma}_{\mu 1}(\mathbf{k}) > E^{\gamma}_{\mu 2}(\mathbf{k})$. This band splitting is induced by the presence of interlayer hopping (i.e., $t_{\mu\mu'}$) and the intrinsic SOC (i.e., λ_μ). After considering the C_3 symmetry for high-symmetric stacking orders in homo-BL TMDs, only the products $|t_{cc}||t_{vv}|$ and $|t_{cv}||t_{vc}|$ are possible and the other terms regarding $|t_{\mu\mu}||t_{\mu\mu'}|$, $|t_{\mu\mu}||t_{\mu'\mu}|$, and $|t_{cc}||t_{cv}||t_{vc}||t_{vv}|$ are

forbidden [32]. Thus, we have

$$b_3 = -(1+\epsilon)\tau s(\lambda_c+\lambda_v), \tag{3a}$$

$$\begin{aligned} b_2 =& -2A^2k^2 - \Delta^2/2 - (1+\epsilon)\tau s\Delta(\lambda_c-\lambda_v)/2 + 2(1+\epsilon)\lambda_c\lambda_v + \epsilon(\lambda_c^2+\lambda_v^2) \\ & - |t_{cc}|^2 - |t_{cv}|^2 - |t_{vc}|^2 - |t_{vv}|^2, \end{aligned} \tag{3b}$$

$$\begin{aligned} b_1 =& A^2k^2(1+\epsilon)\tau s(\lambda_c+\lambda_v) + (1+\epsilon)\tau s\Delta^2(\lambda_c+\lambda_v)/4 + \epsilon\Delta(\lambda_c^2-\lambda_v^2) \\ & - (1+\epsilon)\tau s(\lambda_c^2\lambda_v+\lambda_c\lambda_v^2) - [\Delta - (1+\epsilon)\tau s\lambda_v]|t_{cc}|^2 \\ & + \tau s(\lambda_c+\epsilon\lambda_v)(|t_{cv}|^2+\epsilon|t_{vc}|^2) + [\Delta + (1+\epsilon)\tau s\lambda_c]|t_{vv}|^2, \end{aligned} \tag{3c}$$

$$\begin{aligned} b_0 =& A^4k^4 + A^2k^2\Delta^2/2 + A^2k^2(1+\epsilon)\tau s\Delta(\lambda_c-\lambda_v)/2 - 2A^2k^2\lambda_c\lambda_v \\ & - 2A^2k^2(|t_{cc}||t_{vv}|\cos\phi_1 + |t_{cv}||t_{vc}|\cos\phi_2) + \Delta^4/16 + (1+\epsilon)\tau s\Delta^3(\lambda_c-\lambda_v)/8 \\ & - (1+\epsilon)\Delta^2\lambda_c\lambda_v/2 + \epsilon\Delta^2(\lambda_c^2+\lambda_v^2)/4 - (1+\epsilon)\tau s\Delta(\lambda_c^2\lambda_v-\lambda_c\lambda_v^2)/2 + \lambda_c^2\lambda_v^2 \\ & + (1+\epsilon)\tau s\Delta(\lambda_v|t_{cc}|^2 - \lambda_c|t_{vv}|^2)/2 + \tau s\Delta(\lambda_c-\epsilon\lambda_v)(|t_{cv}|^2+\epsilon|t_{vc}|^2)/2 \\ & - (\Delta^2/4+\epsilon\lambda_v^2)|t_{cc}|^2 + (\Delta^2/4-\epsilon\lambda_c\lambda_v)(|t_{cv}|^2+|t_{vc}|^2) - (\Delta^2/4+\epsilon\lambda_c^2)|t_{vv}|^2 \\ & + |t_{cc}|^2|t_{vv}|^2 + |t_{cv}|^2|t_{vc}|^2. \end{aligned} \tag{3d}$$

Here we define $\phi_1 = \phi_{cc} - \phi_{vv}$ and $\phi_2 = \phi_{cv} - \phi_{vc}$. From Eq. (3), we notice the following features. (i) The electron energy spectrum depends only on k, namely $E^{\gamma}_{\mu\nu}(\mathbf{k}) = E^{\gamma}_{\mu\nu}(k)$, suggesting that it is symmetric along the $\mathbf{k}$ plane; (ii) τ and s appear always in the form of τs so that $E^{\gamma}_{\mu\nu}(k)$ does not depend on τ, implying that the electron energies in K and $K^{'}$ valleys are degenerate but the electronic spins in two valleys are just opposite due to time-reversal symmetry; and (iii) the eigenenergies at the $K/K^{'}$ points (i.e., at $k = 0$) do not depend on the phase angles of the interlayer hopping matrix element. For a specific stacking configuration, the parameters b_j, with $j = 0, 1, 2$, and 3, can be further simplified (see Appendix).

The corresponding eigenfunction for an electron at a state $(\mathbf{k}, \mathscr{B})$ with $\mathscr{B} = (\mu, \nu, \tau, s)$ in six types of high-symmetric BL TMDs is

$$|\mathbf{k}, \mathscr{B}\rangle = \mathcal{A} \begin{pmatrix} c_1 \\ c_2 \\ c_3 \\ c_4 \end{pmatrix} e^{i\mathbf{k}\cdot\mathbf{r}}, \tag{4}$$

where

$$c_1 = -A^3k^2k_\tau^- t_{cc} + A^2k^2h_c^+ t_{cv} + A^2k_{\epsilon\tau}^- k_\tau^- h_c^\epsilon t_{vc} + Ak_\tau^-(A^2k^2 - h_c^\epsilon h_v^\epsilon)t_{cc} \tag{4a}$$
$$- Ak_{\epsilon\tau}^- h_c^+ h_c^\epsilon t_{vv} - h_c^\epsilon t_{cv}|t_{vc}|^2 - (A^2k^2 - h_c^\epsilon h_v^\epsilon)h_c^+ t_{cv},$$
$$c_2 = A^2k_{\epsilon\tau}^+ k_\tau^- h_c^\epsilon t_{cc} - Ak_{\epsilon\tau}^+ h_c^+ h_c^\epsilon t_{cv} - Ak_\tau^- h_c^\epsilon h_c^\epsilon t_{vc} + (h_c^+ h_c^\epsilon - |t_{cc}|^2)h_c^\epsilon t_{vv}, \tag{4b}$$
$$c_3 = Ak_\tau^-(-A^2k^2 + h_c^\epsilon h_v^\epsilon + t_{cc}^* t_{vv} + t_{cv}t_{vc}^*)h_c^\epsilon, \tag{4c}$$
$$c_4 = (A^2k^2 - h_c^\epsilon h_v^\epsilon)h_c^+ h_c^\epsilon + h_c^\epsilon h_v^\epsilon|t_{cc}|^2 + h_c^\epsilon h_c^\epsilon|t_{vc}|^2, \tag{4d}$$

and

$$\mathcal{A} = (|c_1|^2 + |c_2|^2 + |c_3|^2 + |c_4|^2)^{-1/2} \tag{4e}$$

is the normalization coefficient. Here, $h_c^\epsilon = \Delta/2 + \epsilon\tau s\lambda_c - E$, $h_v^\epsilon = -\Delta/2 + \epsilon\tau s\lambda_v - E$, and $h_c^+ = \Delta/2 + \tau s\lambda_c - E$. The specific forms of the eigenfunctions for the studied six types of high-symmetric BL TMDs can be further simplified and the results are shown in Appendix. We note that: (i) the C_3 symmetry for high-symmetric stacking orders in homo-BL TMDs has also been considered here; (ii) although $E_{\mu\nu}^\gamma(\mathbf{k})$ depends only on k, $|\mathbf{k}, \mathscr{B}\rangle$ depends on k_x and k_y generally, indicating that the electron wavefunction is not symmetric along the $\mathbf{k}$ plane; and (iii) $|\mathbf{k}, \mathscr{B}\rangle$ depends generally on the phase angle of the hopping matrix element.

D. Band parameters

In order to obtain the basic band parameters of BL TMD systems, we examine the electronic energy spectrum near each band edge, i.e., $k \to q_{\mu\nu}^\gamma$ the minima/maxima for each conduction/valence subband. From Eq. (3), the electron energy can be expanded as

$$E_{\mu\nu}^\gamma(k) = E_{\mu\nu}^\gamma(q_{\mu\nu}^\gamma) + g_{\mu\nu}^\gamma(k - q_{\mu\nu}^\gamma) + \frac{\hbar^2}{2m_{\mu\nu}^\gamma}(k - q_{\mu\nu}^\gamma)^2 + \alpha_{\mu\nu}^\gamma(k - q_{\mu\nu}^\gamma)^3 + \beta_{\mu\nu}^\gamma(k - q_{\mu\nu}^\gamma)^4 + \cdots, \tag{5}$$

and

$$\begin{aligned}
g_{\mu\nu}^\gamma &= \lim_{k\to q_{\mu\nu}^\gamma} \frac{dE_{\mu\nu}^\gamma(k)}{dk} = \lim_{k\to q_{\mu\nu}^\gamma} k\frac{Q_{\mu\nu}^\gamma(E,k)}{L_{\mu\nu}^\gamma(E,k)}, \\
\frac{\hbar^2}{2m_{\mu\nu}^\gamma} &= \frac{1}{2!}\lim_{k\to q_{\mu\nu}^\gamma} \frac{d^2E_{\mu\nu}^\gamma(k)}{dk^2} = \frac{1}{2!}\lim_{k\to q_{\mu\nu}^\gamma} \frac{J_{\mu\nu}^\gamma(E,k)}{L_{\mu\nu}^\gamma(E,k)}, \\
\alpha_{\mu\nu}^\gamma &= \frac{1}{3!}\lim_{k\to q_{\mu\nu}^\gamma} \frac{d^3E_{\mu\nu}^\gamma(k)}{dk^3} = \frac{1}{3!}\lim_{k\to q_{\mu\nu}^\gamma} \frac{S_{\mu\nu}^\gamma(E,k)}{L_{\mu\nu}^\gamma(E,k)}, \\
\beta_{\mu\nu}^\gamma &= \frac{1}{4!}\lim_{k\to q_{\mu\nu}^\gamma} \frac{d^4E_{\mu\nu}^\gamma(k)}{dk^4} = \frac{1}{4!}\lim_{k\to q_{\mu\nu}^\gamma} \frac{Y_{\mu\nu}^\gamma(E,k)}{L_{\mu\nu}^\gamma(E,k)},
\end{aligned} \tag{6}$$

with

$$L^{\gamma}_{\mu\nu}(E,k) = 4E^3 + 3b_3E^2 + 2b_2E + b_1, \tag{6a}$$

$$\begin{aligned} Q^{\gamma}_{\mu\nu}(E,k) =& 4A^2E^2 - 2A^2(1+\epsilon)\gamma(\lambda_c+\lambda_v)E - 4A^4k^2 \\ & - A^2\Delta^2 - A^2(1+\epsilon)\gamma\Delta(\lambda_c-\lambda_v) + 4A^2\lambda_c\lambda_v \\ & + 4A^2(|t_{cc}||t_{vv}|\cos\phi_1 + |t_{cv}||t_{vc}|\cos\phi_2), \end{aligned} \tag{6b}$$

$$\begin{aligned} J^{\gamma}_{\mu\nu}(E,k) =& -2(6E^2+3b_3E+b_2)(\frac{dE}{dk})^2 - 2[2b_2^{(1)}E + b_1^{(1)}]\frac{dE}{dk} \\ & - b_2^{(2)}E^2 - b_1^{(2)}E - b_0^{(2)}, \end{aligned} \tag{6c}$$

$$\begin{aligned} S^{\gamma}_{\mu\nu}(E,k) =& -6(6E^2+3b_3E+b_2)\frac{dE}{dk}\frac{d^2E}{dk^2} - 3[2b_2^{(1)}E + b_1^{(1)}]\frac{d^2E}{dk^2} \\ & - 6(4E+b_3)(\frac{dE}{dk})^3 - 6b_2^{(1)}(\frac{dE}{dk})^2 - 3[2b_2^{(2)}E + b_1^{(2)}]\frac{dE}{dk} \\ & - b_0^{(3)}, \end{aligned} \tag{6d}$$

$$\begin{aligned} Y^{\gamma}_{\mu\nu}(E,k) =& -8(6E^2+3b_3E+b_2)\frac{dE}{dk}\frac{d^3E}{dk^3} - 4[2b_2^{(1)}E + b_1^{(1)}]\frac{d^3E}{dk^3} \\ & - 6(6E^2+3b_3E+b_2)(\frac{d^2E}{dk^2})^2 - 36(4E+b_3)(\frac{dE}{dk})^2\frac{d^2E}{dk^2} \\ & - 24b_2^{(1)}\frac{dE}{dk}\frac{d^2E}{dk^2} - 6[2b_2^{(2)}E + b_1^{(2)}]\frac{d^2E}{dk^2} - 24(\frac{dE}{dk})^4 \\ & - 12b_2^{(2)}(\frac{dE}{dk})^2 - b_0^{(4)}, \end{aligned} \tag{6e}$$

where $E^{\gamma}_{\mu\nu}(q^{\gamma}_{\mu\nu})$ is the band edge, $m^{\gamma}_{\mu\nu}$ is the effective band quality or mass, $\alpha^{\gamma}_{\mu\nu}$ is the third-order correction, $\beta^{\gamma}_{\mu\nu}$ is the fourth-order correction, d^nE/dk^n represents $d^nE^{\gamma}_{\mu\nu}(k)/dk^n$, and $b_j^{(n)} = d^nb_j/dk^n$ with $j = 0, 1, 2,$ and 3.

E. Electron density-of-states

From electronic energy spectrum of a BL TMD, we can calculate the Green's function for a free electron in the system through [40]

$$G(\mathcal{E}) = P\Big(\frac{1}{\mathcal{E} - E(\mathbf{k})}\Big) - i\pi\delta[\mathcal{E} - E(\mathbf{k})], \tag{7}$$

with P being the principal value and $\mathcal{E}$ the electron energy. Thus, we can determine the electron density-of-states (DoS) for BL TMD system from the imaginary part of the Green's

function, which reads

$$D_c(\mathcal{E}) = \sum_{\gamma,\nu} D^{\gamma}_{c\nu}(\mathcal{E}) = \frac{g_\gamma}{2\pi} \sum_{\gamma,\nu} \sum_i \Theta[\mathcal{E} - E^{\gamma}_{c\nu}(q^{\gamma}_{c\nu})] \frac{k_i}{|dE^{\gamma}_{c\nu}(k)/dk|_{k=k_i}},$$
$$D_v(\mathcal{E}) = \sum_{\gamma,\nu} D^{\gamma}_{v\nu}(\mathcal{E}) = \frac{g_\gamma}{2\pi} \sum_{\gamma,\nu} \sum_i \Theta[E^{\gamma}_{v\nu}(q^{\gamma}_{v\nu}) - \mathcal{E}] \frac{k_i}{|dE^{\gamma}_{v\nu}(k)/dk|_{k=k_i}}, \tag{8}$$

for conduction and valence band respectively, where $g_\gamma = 2$ because $\gamma = +$ for $(\tau, s) = (\pm, \pm)$ and $\gamma = -$ for $(\tau, s) = (\pm, \mp)$, $\Theta(x)$ is a unit step function, and k_i is the ith solution for k from the equation $\mathcal{E} - E^{\gamma}_{\mu\nu}(k) = 0$.

Through Eqs. (6) and (8), it can be written as

$$D_c(\mathcal{E}) = D_0 \frac{\hbar^2}{m_0} \sum_{\gamma,\nu} \sum_i \Theta[\mathcal{E} - E^{\gamma}_{c\nu}(q^{\gamma}_{\mu\nu})] \left| \frac{L^{\gamma}_{\mu\nu}(\mathcal{E}, k_i)}{Q^{\gamma}_{\mu\nu}(\mathcal{E}, k_i)} \right|,$$
$$D_v(\mathcal{E}) = D_0 \frac{\hbar^2}{m_0} \sum_{\gamma,\nu} \sum_i \Theta[E^{\gamma}_{v\nu}(q^{\gamma}_{\mu\nu}) - \mathcal{E}] \left| \frac{L^{\gamma}_{\mu\nu}(\mathcal{E}, k_i)}{Q^{\gamma}_{v\nu}(\mathcal{E}, k_i)} \right|, \tag{9}$$

where $D_0 = g_\gamma m_0/(2\pi\hbar^2)$ and m_0 is the rest electron mass.

F. The Fermi energy

From electron DoS, we can determine the Fermi energy (E_F) or chemical potential in a BL TMD structure. For n-type BL TMDs, after applying the condition of electron number conservation, we have

$$n_e = \int_{E_b}^{\infty} dE D_c(E) f(E) = g_\gamma \sum_{\gamma,\nu,\mathbf{k}} f[E^{\gamma}_{c\nu}(\mathbf{k})], \tag{10}$$

with n_e being the electron density, $f(E) = [e^{(E-E_F)/k_BT} + 1]^{-1}$ the Fermi-Dirac function, and E_b the bottom of the conduction band. At low-temperature limit (i.e., $T \to 0$), we have $f(E) \to \Theta(E_F - E)$ and, thus,

$$n_e = g_\gamma \sum_{\gamma,\nu,\mathbf{k}} f[E^{\gamma}_{c\nu}(\mathbf{k})] = 2 \sum_{\gamma,\nu} \frac{k^2_F(\gamma,\nu)}{4\pi}, \tag{10a}$$

where $k_F(\gamma,\nu)$ is the Fermi wavevector, which is the solution for k from $E_F - E^{\gamma}_{c\nu}(k) = 0$.

III. RESULTS AND DISCUSSIONS

In this study, we take BL MoS_2 as an example to discuss the electronic band structure in six types of high-symmetric homo-BL TMD systems. The material parameters for MoS_2

TABLE I: $|t_{\mu\mu'}|$ (in meV) in six types of high-symmetric BL MoS_2.

	H^M_M	H^M_X	H^X_X	R^M_M	R^M_X	R^X_M
$\|t_{cc}\|$	25	0	0	25	0	0
$\|t_{cv}\|$	0	0	30	0	0	30
$\|t_{vc}\|$	0	0	30	0	30	0
$\|t_{vv}\|$	0	43	0	35	0	0

used in the numerical calculation are [5, 6, 29, 41]: $a = 3.193$ Å, $t = 1.10$ eV, $\Delta = 1.66$ eV, $\lambda_c = -1.5$ meV, and $\lambda_v = 75$ meV. To conduct the numerical calculations, we also need to know the values of the hopping matrix elements $t_{\mu\mu'}$. We note the following points. (i) As been pointed out [6, 35], in order to satisfy the C_3 symmetry some of the interlayer hopping transitions are forbidden so that the corresponding $t_{\mu\mu'} = 0$ (see Appendix G). (ii) It is known that the center-inversion symmetry can lead to $E^{\gamma}_{\mu\nu}(\mathbf{k}) = E^{\gamma'}_{\mu\nu}(\mathbf{k})$ with $\gamma = \tau s$, and $\gamma' = (-\tau)s$ and the time-reversal symmetry can result in $E^{\gamma}_{\mu\nu}(\mathbf{k}) = E^{\gamma'}_{\mu\nu}(\mathbf{k})$ with $\gamma' = (-\tau)(-s)$. For the case where both of them are satisfied, $E^{\gamma}_{\mu\nu}(\mathbf{k}) = E^{\gamma'}_{\mu\nu}(\mathbf{k})$ with $\gamma' = \tau(-s)$. Therefore, $E^{+}_{\mu\nu}(k) = E^{-}_{\mu\nu}(k)$ in H-stacked BL TMDs, which means γ does not affect $E^{\gamma}_{\mu\nu}(k)$ and τs disappears in Eq. (3). Thereby, $|t_{cv}| = |t_{vc}|$ in H^X_X (see Appendix C). (iii) R^M_X is the case of operating the out-of-plane mirror symmetry on R^X_M, which means their band structures should be the same. As a result, $|t_{vc}|$ for R^M_X is equal to $|t_{cv}|$ R^X_M (see Appendix F). And (iv) the values of $|t_{\mu\mu'}|$ for H^M_X [23] and R^M_M [35] were already obtained by the DFT calculations. It should be noted that the actual values of $|t_{\mu\mu'}|$ are not easy to evaluate quantitatively because they are affected by both the in-plane transitions [35] and the out-of-plane interlayer hopping. Through referring to the known $|t_{\mu\mu'}|$, we take $|t_{cc}| = 25$ meV for H^M_M and $|t_{cv}| = |t_{vc}| = 30$ meV for H^X_X, R^M_X and R^X_M in the calculations. The values of $|t_{\mu\mu'}|$ used in our calculations are shown in Table I. The zero values of $|t_{\mu\mu'}|$ shown in Table I are the consequence of the C_3 symmetry. From this Table and the first term in the second line of Eq. (3d), we find ϕ_1 only affects R^M_M and ϕ_2 only affects H^X_X. At present, we do not know the values of ϕ_1 and ϕ_2 for BL MoS_2 and we take them as input parameters.

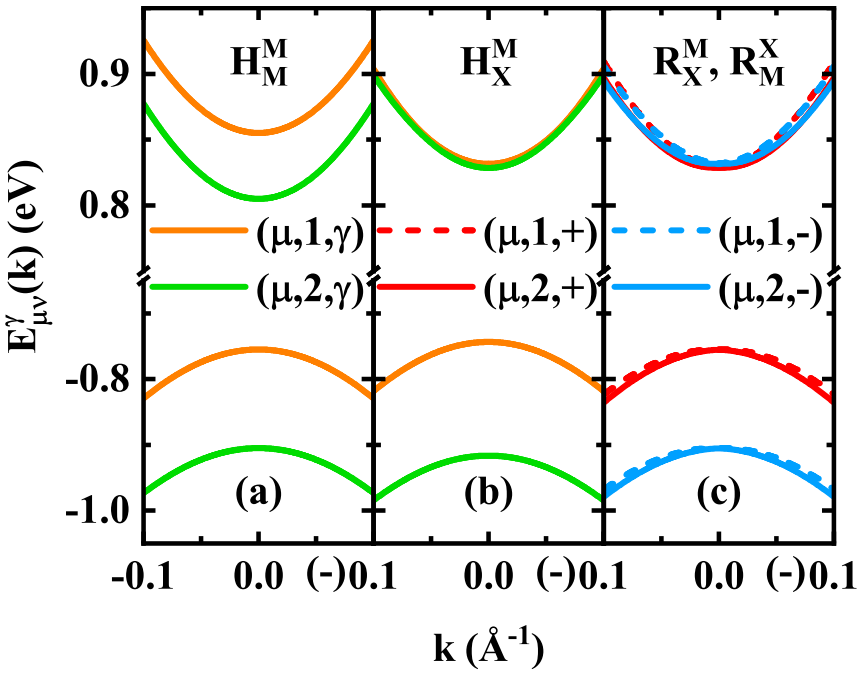

FIG. 2: The electron energy spectra in four types of high-symmetric BL MoS_2, as indicated. Here (μ, ν, γ) denotes $E^{\gamma}_{\mu\nu}(k)$.

A. Electronic band structure

In Fig. 2, we show the electronic energy dispersion in H^M_M, H^M_X, R^M_X, and R^X_M stacking structures of BL MoS_2, where $E^{\gamma}_{\mu\nu}(k)$ is independent upon the phase angle of the hopping matrix elements and $E^{\gamma}_{\mu\nu}(k)$ for R^M_X and R^X_M stacking orders are the same. In Figs. 3 and 4, we show respectively the electron energy spectra in H^X_X and R^M_M stacking BL MoS_2 for different phase angles ϕ_2 and ϕ_1 induced by the phases of interlayer hopping matrix elements. In the presence of intrinsic SOC in ML TMD and of the interlayer hopping in BL TMD, one would think that the band splitting can be observed in BL TMD structures. However, because a homo-BL structure should satisfy the lattice symmetry, the band splitting in some stacking structures can be suppressed. In Figs. 2 and 3, each curve of energy spectrum for H-stacking BL is fourfold degeneracy because of center-inversion symmetry and time-reversal symmetry so that $E^{\gamma}_{\mu\nu}(k) = E^{-\gamma}_{\mu\nu}(k)$ with $\gamma = s\tau$, whereas the subbands with different colors (or ν) are not degenerate. For the case of R stacking, each curve in Figs. 2 and 4 is twofold degeneracy because of time-reversal symmetry only so that $E^{s\tau}_{\mu\nu}(k) = E^{(-s)(-\tau)}_{\mu\nu}(k)$, whereas the subbands with different colors (γ) or curve styles (ν) are not degenerate. For the case

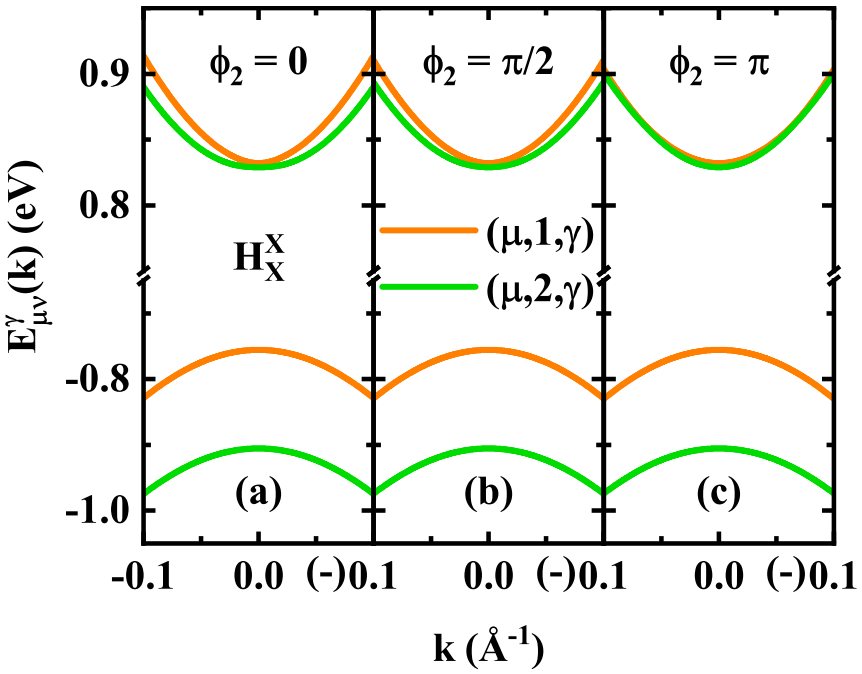

FIG. 3: The electron energy spectra in H_X^X stacked BL MoS_2, as indicated. Here (μ, ν, γ) denotes $E^{\gamma}_{\mu\nu}(k)$.

of $t_{\mu\mu'} = 0$, the intrinsic SOC causes $E^{\gamma}_{\mu 1}(0) - E^{\gamma}_{\mu 2}(0) = 2|\lambda_\mu|$ and $E^{+}_{\mu\nu}(0) - E^{-}_{\mu\nu}(0) = 0$ in H-stacked BL, whereas $E^{\gamma}_{\mu 1}(0) - E^{\gamma}_{\mu 2}(0) = 0$ and $|E^{+}_{\mu\nu}(0) - E^{-}_{\mu\nu}(0)| = 2|\lambda_\mu|$ in R-stacked BL. Therefore, the intrinsic SOC can cause the band splitting. For the case of $\lambda_\mu = 0$, the intraband interlayer hopping causes $E^{\tau}_{\mu 1}(0) - E^{\tau}_{\mu 2}(0) = 2|t_{\mu\mu}|$ and the interband interlayer hopping causes $E^{\tau}_{c1}(0) - E^{\tau}_{v2}(0) - \Delta \approx 2|t_{\mu\mu'}|^2/\Delta$. Thus, the interlayer hopping can also induce the band splitting. Because $|t_{\mu\mu'}| \ll \Delta$, the band splitting induced by interband interlayer hopping is much weaker than that induced by intraband interlayer hopping. For H_X^X stacking in Fig. 3, ϕ_2 affects $E^{\gamma}_{\mu\nu}(k)$ rather markedly in the conduction band and a very weak effect of ϕ_2 can be seen in the valence band. For R_M^M stacking in Fig. 4, ϕ_1 affects $E^{\gamma}_{\mu\nu}(k)$ rather weakly. Furthermore, we find that for R_X^M and R_M^X stacking orders, $E^{-}_{v2}(0) < E^{-}_{v1}(0) < E^{+}_{v2}(0) < E^{+}_{v1}(0) < E^{+}_{c2}(0) < E^{+}_{c1}(0) < E^{-}_{c2}(0) < E^{-}_{c1}(0)$.

To see more clearly the influence of phase angle of the hopping matrix elements on $E^{\gamma}_{\mu\nu}(k)$, in Figs. 5 and 6 we show respectively the energy differences $\Delta^{\gamma}_{\mu}(k) = E^{\gamma}_{\mu 1}(k) - E^{\gamma}_{\mu 2}(k)$ in H_X^X and R_M^M stacked BL MoS_2 for different ϕ_2 and ϕ_1 phase angles. For H_X^M and for H_X^X with ϕ_2 larger than $\approx 155^o$, $\Delta^{\gamma}_{c}(k)$ are not monotonic, which decreases first then increases with increasing k. When $\phi_2 \approx 155°$, $\Delta^{\gamma}_{c}(k)$ is almost unchanged ($\approx$ 3 meV) as $k < 0.5$

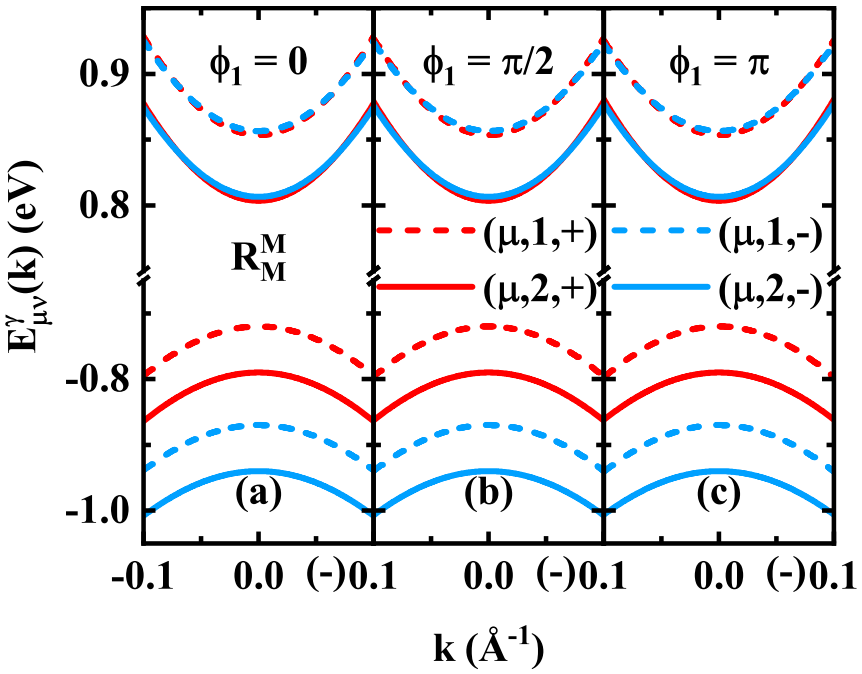

FIG. 4: The electron energy spectra in R^M_M stacked BL MoS_2, as indicated. Here (μ, ν, γ) denotes $E^{\gamma}_{\mu\nu}(k)$.

Å^{-1}, implying that the optoelectronic properties of this structure near the K/K$'$ valley are sensitive to terahertz (THz) radiation ($f = 1$ THz $\Leftrightarrow$ 4.13 meV). We see that ϕ_2 affects $\Delta^{\gamma}_c(k)$ more strongly than $\Delta^{\gamma}_v(k)$ as shown in Fig. 5. For R^M_M stacking, due to the presence of spin-split subbands (see Fig. 4), $\Delta^{+}_{\mu}(k)$ differs from $\Delta^{-}_{\mu}(k)$ and, as a result, there are two curves with the same color in both conduction and valence bands in Fig. 6. The same figure further shows that $\partial[\Delta^{+}_{\mu}(k) - \Delta^{-}_{\mu}(k)]/\partial\phi_1 < 0$.

It should be noticed that ML TMD was often considered to satisfy the in-plane mirror symmetry so that the six types of high-symmetric homo-BL TMDs were thought to satisfy this symmetry as well. Thus, ϕ_1 and ϕ_2 could be taken as zero [36]. However, the discovery of the Ising superconductivity in gated MoS_2 in 2015 [37] suggests that the in-plane mirror symmetry can be broken in both ML and BL TMDs. Therefore, ϕ_1 and ϕ_2 may not be zero in some high symmetric homo-BL TMDs. We find that the phase angles in the hopping matrix elements can only affect the electronic band structures in R^M_M and H^X_X stacked BL MoS_2 due to the satisfaction of the structure symmetry.

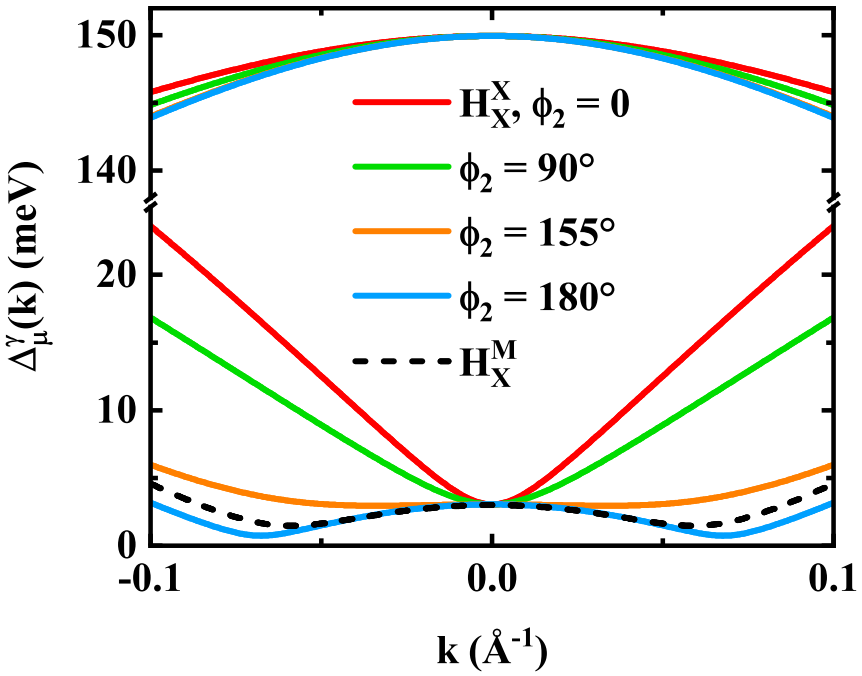

FIG. 5: The energy difference $\Delta^{\gamma}_{\mu}(k)$ in H^{X}_{X} stacked BL MoS_2 at different ϕ_2, as indicated. The dashed black curve shows $\Delta^{\gamma}_{c}(k)$ for H^{M}_{X} stacking for comparison. The curves in the upper (lower) part of the panel are the results for the valence (conduction) band.

TABLE II: Δ_g (in meV) in six types of high-symmetric BL MoS_2.

	H^{M}_{M}	H^{M}_{X}	H^{X}_{X}	R^{M}_{M}	R^{M}_{X}/R^{X}_{M}
Δ_g	23.6	11.5	-1.1	60	0

B. Band parameters

Our numerical results shown in Figs. 2 - 4 indicate that the band edges in six types of high-symmetric stacking BL MoS_2 are all located at $k = 0$, i.e. $q^{\gamma}_{\mu\nu} = 0$ in Eq. (5). This can also be proven by $g^{\gamma}_{\mu\nu} = \lim_{k\to 0} dE^{\gamma}_{\mu\nu}/dk = 0$. We define $\Delta_{SOC} = \Delta + \lambda_c - \lambda_v$ as the band gap in ML MoS_2 with SOC. In the presence of interlayer hopping, the band gap for BL MoS_2 with SOC becomes Δ_{BL}, which is the difference between the lowest conduction subband and the highest valence subband at $k = 0$. The band gap difference is $\Delta_g = \Delta_{SOC} - \Delta_{BL}$. From our numerical results for BL MoS_2, we find: (i) $\Delta_{SOC} > \Delta_{BL}$ in H^{M}_{M}, H^{M}_{X}, and R^{M}_{M} stacking orders, which means the red shift of the main exciton peaks at the K/K$'$ valley in the three BL stacking orders [15, 16]; (ii) $\Delta_{SOC} = \Delta_{BL}$ in R^{M}_{X} and R^{X}_{M} stacking orders, which means

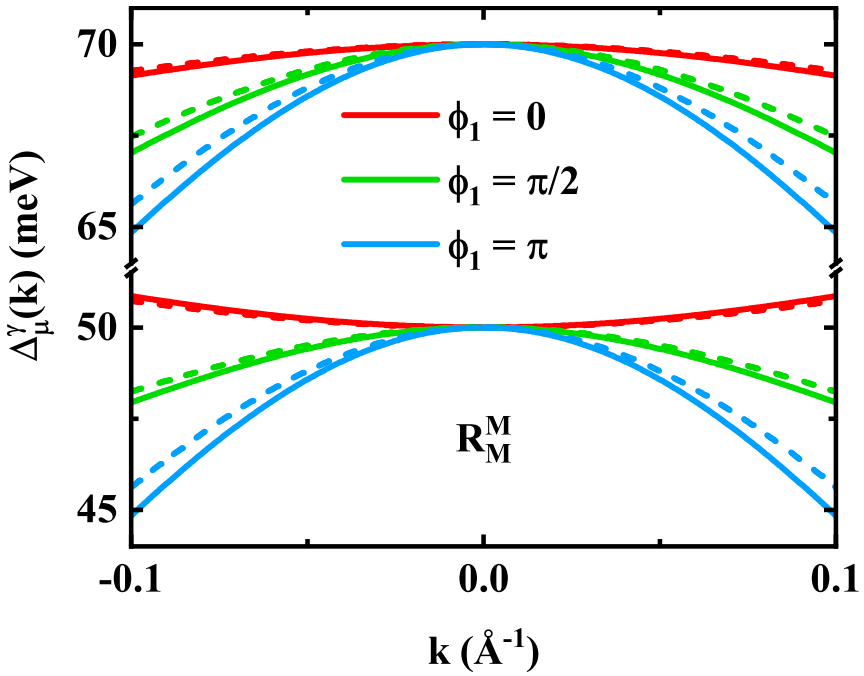

FIG. 6: The energy difference $\Delta^{\gamma}_{\mu}(k)$ in $\mathrm{R^M_M}$ stacked BL MoS_2 at different ϕ_1, as indicated. The curves in the upper (lower) part of the panel are the results for the valence (conduction) band. The solid/dashed curves denote the spin-up/down states.

the positions of the main exciton peaks at the K/K$'$ valley are almost unchanged in the two BL stacking orders [16, 26]; and (iii) $\Delta_{SOC} < \Delta_{BL}$ in $\mathrm{H^X_X}$ stacking order because of the efforts of the interlayer hopping matrix elements t_{cv} and t_{vc}. The values of Δ_g for six types of high-symmetric BL MoS_2 are summoned in Table II, for facilitated visualization that different stacking configurations have different BL band gaps.

From Eqs. (6d) and (3a) - (3d), we see that $\lim_{k\to 0} S^{\gamma}_{\mu\nu}(E,k) = 0$. Thus, $\alpha^{\gamma}_{\mu\nu} = 0$ so that there is no third-order correction in Eq. (5) for BL MoS_2. Using Table I, we have $J^{\gamma}_{v1}[E^{\gamma}_{v1}(0),0] = J^{\gamma}_{c2}[E^{\gamma}_{c2}(0),0] = 0$ for $\mathrm{R^M_X}$ and $\mathrm{R^X_M}$ stacking structures and

$$\begin{aligned} L^{\gamma}_{v1}[E^{\gamma}_{v1}(0),0] &= -L^{\gamma}_{c2}[E^{\gamma}_{c2}(0),0] = |t_{vc}|^2(\Delta + \gamma\lambda_c - \gamma\lambda_v), \text{ for } \mathrm{R^M_X}, \\ L^{\gamma}_{v1}[E^{\gamma}_{v1}(0),0] &= -L^{\gamma}_{c2}[E^{\gamma}_{c2}(0),0] = |t_{cv}|^2(\Delta + \gamma\lambda_c - \gamma\lambda_v), \text{ for } \mathrm{R^X_M}, \end{aligned} \tag{11}$$

in Eq. (6). The values of $m^{\gamma}_{\mu\nu}/m_0$, with m_0 being the rest electron mass, and $\beta^{\gamma}_{\mu\nu}$ in Eq. (5) are shown respectively in Tables III and IV. On the basis of Eqs. (5) and (6), we note the following points: (i) Because $J^{\gamma}_{v1}[E^{\gamma}_{v1}(0),0] = J^{\gamma}_{c2}[E^{\gamma}_{c2}(0),0] = 0$ for $\mathrm{R^M_X}$ and $\mathrm{R^X_M}$ stacking structures, $\hbar^2/(2m^{\gamma}_{c2}) \to 0$ and $\hbar^2/(2m^{\gamma}_{v1}) \to 0$, implying that $m^{\gamma}_{c2} \to \infty$ and

TABLE III: The effective band mass $m^{\gamma}_{\mu\nu}/m_0$ at the band edge in six types of high-symmetric BL MoS_2. Here, (μ,ν,γ) represents $E^{\gamma}_{\mu\nu}(k)$ and the effect of (ϕ_1,ϕ_2) on $m^{\gamma}_{\mu\nu}$ for $(\mathrm{R^M_M},\mathrm{H^X_X})$ structure is indicated.

			$\mathrm{H^X_X}$ (ϕ_2)			$\mathrm{R^M_M}$ (ϕ_1)			
	$\mathrm{H^M_M}$	$\mathrm{H^M_X}$	0	$\pi/2$	π	0	$\pi/2$	π	$\mathrm{R^M_X/R^X_M}$
$(c,1,+)$	0.521	0.536	0.307	0.391	0.536	0.486	0.497	0.508	0.245
$(c,1,-)$	0.521	0.536	0.307	0.391	0.536	0.533	0.544	0.555	0.268
$(c,2,+)$	0.502	0.489	1.540	0.744	0.490	0.492	0.481	0.471	∞
$(c,2,-)$	0.502	0.489	1.540	0.744	0.490	0.539	0.528	0.518	∞
$(v,1,+)$	-0.489	-0.486	-0.497	-0.493	-0.489	-0.486	-0.478	-0.471	∞
$(v,1,-)$	-0.489	-0.486	-0.497	-0.493	-0.489	-0.533	-0.525	-0.518	∞
$(v,2,+)$	-0.536	-0.540	-0.529	-0.533	-0.537	-0.492	-0.500	-0.508	-0.245
$(v,2,-)$	-0.536	-0.540	-0.529	-0.533	-0.537	-0.539	-0.547	-0.555	-0.268

$m^{\gamma}_{v1}\to\infty$ and the energy dispersion comes mainly from the k^4 term; (ii) comparing with the effective electron masses $m^*/m_0\sim 0.5$ at the edges of conduction and valence bands for ML MoS_2 obtained from DFT calculations [6], the effective band masses for $\mathrm{H^M_M}$, $\mathrm{H^M_X}$ and $\mathrm{R^M_M}$ stacking BL MoS_2 do not differ significantly from this value; and (iii) for $\mathrm{R^M_M/H^X_X}$ stacking, the dependence of $m^{\gamma}_{\mu\nu}$ and $\beta^{\gamma}_{\mu\nu}$ upon ϕ_1/ϕ_2 can be clearly seen.

C. The electron density-of-states

From Eq. (9), we can find the singular point in electron DoS at $\mathrm{K/K'}$ point (i.e., at $k=0$) in BL MoS_2. Letting $\lim_{k\to 0} Q^{\gamma}_{\mu\nu}(E_0,k)=0$, we can get E_0 and then find the singular point when $E_0=E^{\gamma}_{\mu\nu}(0)$. Since

$$\lim_{k\to 0} Q^{\gamma}_{\mu\nu}(E_0,k)/A^2 = \lim_{k\to 0} 4E^2 - 2\gamma(1+\epsilon)(\lambda_c+\lambda_v)E - 4A^2k^2 - \Delta^2 - \gamma(1+\epsilon)\Delta(\lambda_c-\lambda_v) + 4\lambda_c\lambda_v + 4(|t_{cc}||t_{vv}|\cos\phi_1 + |t_{cv}||t_{vc}|\cos\phi_2) = 0, \quad (12)$$

we find that there are two singular points at $E_0=-\Delta/2+\gamma\lambda_v=E^{\gamma}_{v1}(0)$ and $E_0=\Delta/2+\gamma\lambda_c=E^{\gamma}_{c2}(0)$ for $\mathrm{R^M_X}$ and $\mathrm{R^X_M}$ stacking structures so that $D_c(\Delta/2+\gamma\lambda_c)=\infty$, and $D_v(-\Delta/2+\gamma\lambda_v)=\infty$. There is no singular point in other stacking orders.

TABLE IV: The fourth-order correction parameter, $\beta^{\gamma}_{\mu\nu}$ in units of eVÅ^4, at the band edge in six types of high-symmetric BL MoS_2. Here (μ, ν, γ) represents $E^{\gamma}_{\mu\nu}(k)$ and the effect of (ϕ_1, ϕ_2) on $\beta^{\gamma}_{\mu\nu}$ for (R^M_M, H^X_X) structure is indicated.

			H^X_X (ϕ_2)			R^M_M (ϕ_1)			
	H^M_M	H^M_X	0	$\pi/2$	π	0	$\pi/2$	π	R^M_X/R^X_M
$(c, 1, +)$	-29.7	-16.8	-8153.2	-1793.7	-26.9	-39.1	-36.1	-34.3	-106860.3
$(c, 1, -)$	-29.7	-16.8	-8153.2	-1793.7	-26.9	-29.6	-27.5	-26.2	-97433.3
$(c, 2, +)$	-37.8	-50.9	8086.5	1726.7	-40.4	-37.6	-40.9	-43.0	106783.9
$(c, 2, -)$	-37.8	-50.9	8086.5	1726.7	-40.4	-28.6	-30.8	-32.3	97375.4
$(v, 1, +)$	38.5	39.2	36.4	37.4	38.2	39.1	41.3	43.0	-106783.9
$(v, 1, -)$	38.5	39.2	36.4	37.4	38.2	29.6	31.1	32.3	-97375.4
$(v, 2, +)$	29.0	28.5	30.3	29.6	29.0	37.6	35.7	34.3	106860.3
$(v, 2, -)$	29.0	28.5	30.3	29.6	29.0	28.6	27.3	26.2	97433.3

In Figs. 7, 8, and 9, we show the electron DoS in six types of high-symmetric BL MoS_2 as a function of the electron energy E. It is known that for an ideal 2DES with a parabolic energy spectrum, the electron DoS is a unit-step function [42]. In contrast, the electron DoSs in high-symmetric BL MoS_2 do not show this feature, indicating that the corresponding electronic energy spectra are nonparabolic. Once again, the electron DoS in (H^X_X, R^M_M) stacking order depends on the phase angle (ϕ_2, ϕ_1).

D. The Fermi energy

We use Eq. (10) to evaluate the Fermi energy in n-type BL MoS_2 with six types of high symmetries at temperature $T \to 0$. In Figs. 10, 11, and 12, we plot the Fermi energy as a function of the electron density n_e in n-type BL MoS_2 respectively. For H-stacking structures, because the subband energies are spin degenerate [see Figs. 2(a), 2(b), and 3], $(\nu, \gamma) = (2, \gamma)$ states are occupied by electrons first and, with increasing n_e, the higher energy $(1, \gamma)$ can become populated. For R^M_M stacked BL TMDs, because of the spin splitting of the subband energies (see Fig. 4), $(2, +)$ states are occupied first and then $(2, -)$, $(1, +)$, and $(1, -)$ states become populated respectively with increasing n_e. In contrast, for R^M_X and R^X_M

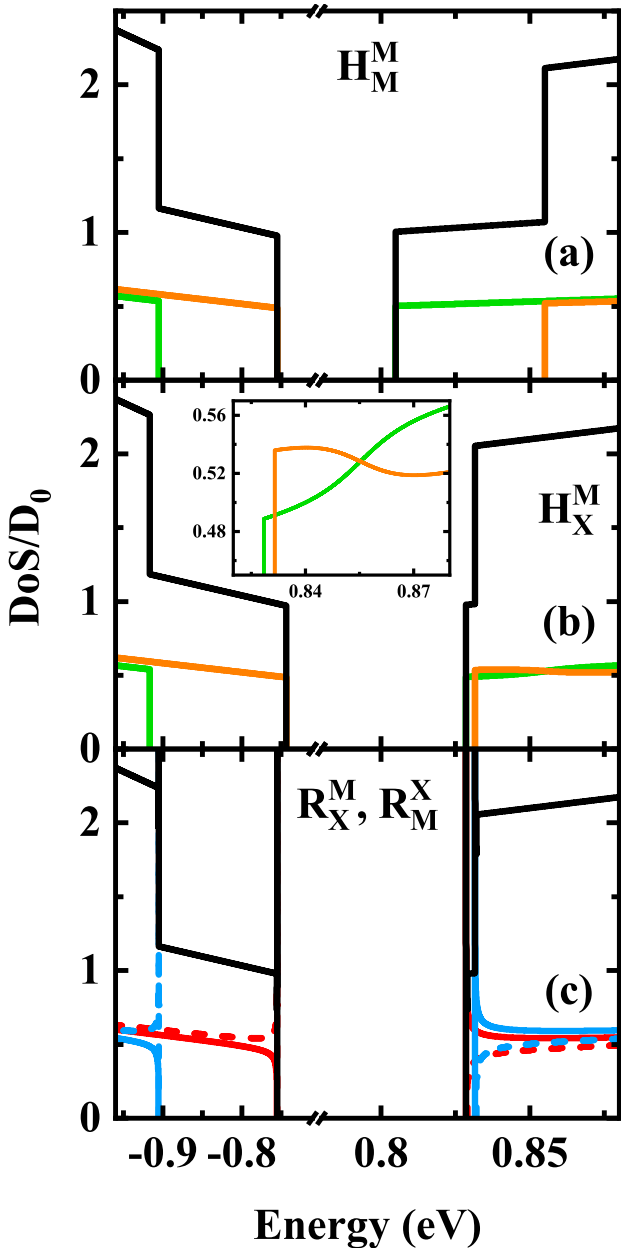

FIG. 7: The electron DoS in four types of high-symmetric BL MoS_2, as indicated. The legends are the same as in Fig. 8 and Fig. 9. The inset shows the DoS around the conduction band edge.

stacking orders [see Fig. 2(c)], $(2,+)$ states are occupied first and then $(1,+)$, $(2,-)$, and $(1,-)$ states become populated respectively with increasing n_e. These features are consistent with the electron energy levels shown in Figs. 2 - 4. Moreover, we find that E_F increases with ϕ_1 (ϕ_2) up to $n_e \sim 3\times10^{13}$ cm^{-2} in R^M_M (H^X_X) stacked BL TMDs, as a consequence of the dependence of the corresponding electron energies upon the phase angles of the hopping matrix elements.

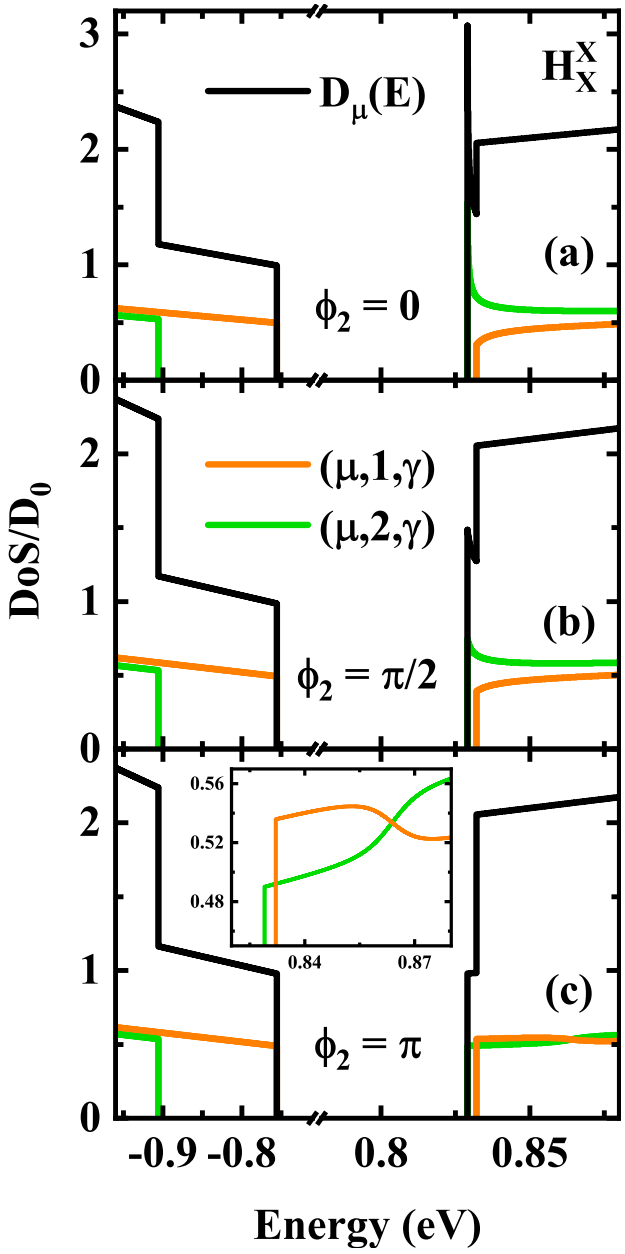

FIG. 8: The electron DoS in H_X^X stacked BL MoS_2. (μ, ν, γ) denotes $D^{\gamma}_{\mu\nu}(E)$. The inset shows the DoS around the conduction band edge.

It is known that the dependence of the Fermi energy upon the electron density directly reflects the features of the electron DoS [see Eq. (10)]. For a n-type BL MoS_2, the DoS $D_c(E)$ exists immediately when $E \geq E_b$ the bottom of the conduction band (see Figs. 7 - 9) so that the electrons are populated in the conduction band and the Fermi level is established. In general, E_F increases with n_e because more electrons have to occupy the higher-energy states. For six types of high-symmetric homo-BL MoS_2, the slope of the increase in E_F with

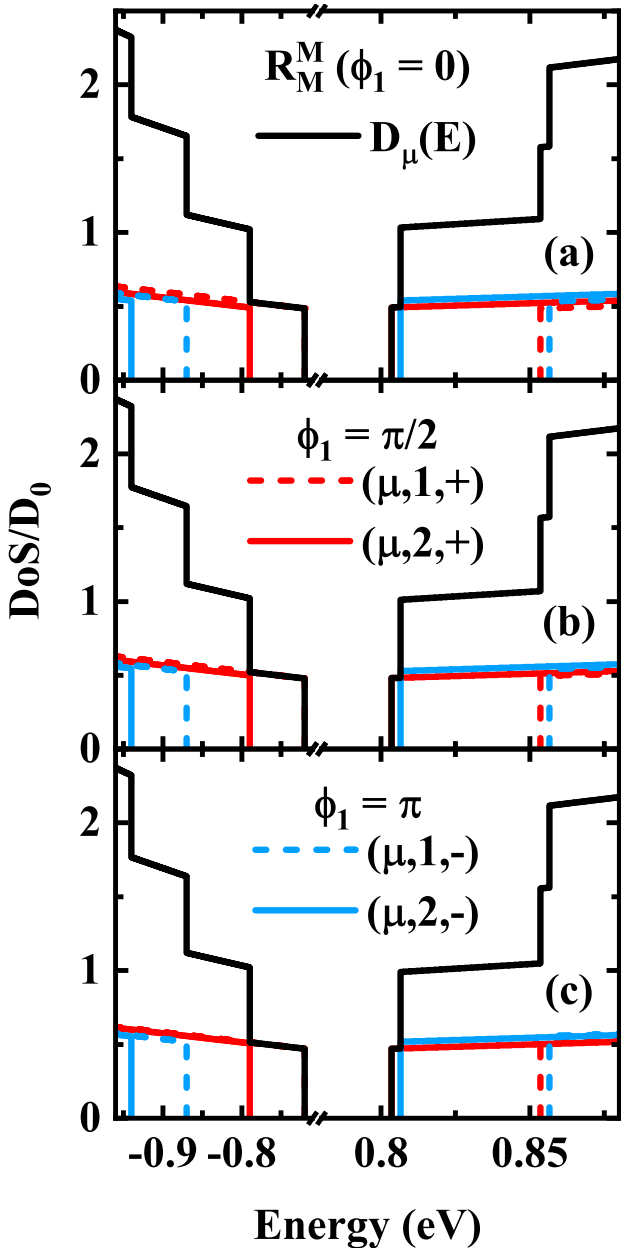

FIG. 9: The electron DoS in R_M^M stacked BL MoS_2. (μ, ν, γ) denotes $D^{\gamma}_{\mu\nu}(E)$.

increasing n_e depends on the dependence of $D_c(E)$ upon the electron energy. It is interesting to notice that in contrast to a semiconductor-based quantum well system (QWS) in which the DoS is the unit-step function like, the DoS for six types of high-symmetric homo-BL MoS_2 is the functional form of electron energy E. Therefore, the dependence of E_F upon n_e here differs from that in a semiconductor-based QWS.

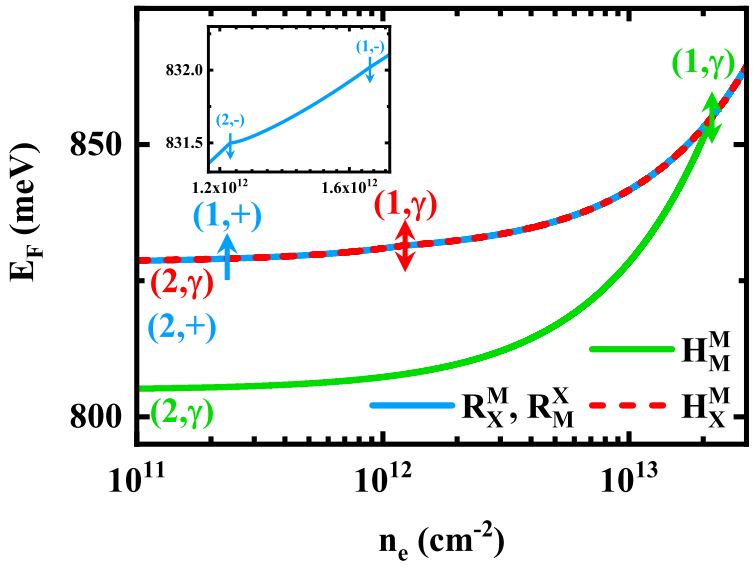

FIG. 10: The Fermi energy in four types of high-symmetric BL MoS_2, as indicated, as a function of electron density. Here (ν, γ) is the position of $E^{\gamma}_{c\nu}(0)$ and $\uparrow$ ($\downarrow$) denotes $\gamma = +$ ($-$). The inset shows the E_F around $E^{-}_{c2}(0)$ and $E^{-}_{c1}(0)$ in $\mathrm{R^M_X}$ and $\mathrm{R^X_M}$ stacking BL MoS_2.

IV. CONCLUSIONS

In this paper, we have systematically analyzed the electronic band structure of six types of high-symmetric BL TMDs, namely $\mathrm{H^M_M}$, $\mathrm{H^M_X}$, $\mathrm{H^X_X}$, $\mathrm{R^M_M}$, $\mathrm{R^M_X}$, and $\mathrm{R^X_M}$ ones, exploiting the practical and analytical convenience of the $k \cdot p$ approach. The electron Hamiltonian for BL TMDs has been constructed on the basis of ML TMDs in the presence of interlayer hopping. The phase angle of the hopping matrix elements has been considered. In this way, we have conveniently obtained the electronic energy spectrum, the electron wave function, the band parameters, the electron density of states, and the Fermi energy in the BL TMD structures of interest. Furthermore, we applied the methodology specifically to BL MoS_2 as a useful example to evaluate and examine the features of the above listed electronic properties. The main conclusions obtained from this study are summarized as follows.

(1) High-symmetric BL TMDs include three types of center-inversion-symmetric H-stacked BL and three types of R-stacked BL orders. They all maintain time-reversal symmetry. Among them, the electronic band structure only in $\mathrm{R^M_M}$ and $\mathrm{H^X_X}$ stacking orders depends on the phase angle of the interlayer hopping matrix elements. Furthermore, $\mathrm{R^M_X}$ and $\mathrm{R^X_M}$ stacked BL TMDs are with the same electronic energy spectrum but their electron

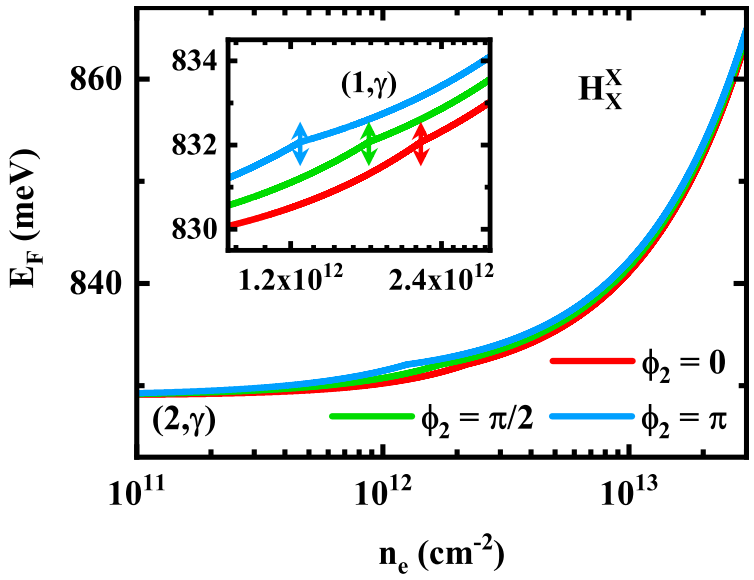

FIG. 11: The Fermi energy in H_X^X stacking BL MoS_2 as a function of electron density for different ϕ_2 angles as indicated. (ν, γ) is the position of $E_{c\nu}^{\gamma}(0)$ and $\uparrow$ ($\downarrow$) denotes $\gamma = +$ ($-$). The inset shows the details of ϕ_2 dependence of E_F around $E_{c1}^{\gamma}(0)$.

wavefunctions are different.

(2) For the H_X^X stacking order, ϕ_2 affects significantly the energy difference between electronic subbands, effective band masses, fourth-order correction parameter, electron DoS, and Fermi energy. In comparison, ϕ_1 affects relatively weakly the electronic band structure in R_M^M stacked BL TMDs.

(3) Interestingly, although the intrinsic SOC can lead to spin splitting in electronic band in ML TMDs, this band splitting can be suppressed in H-stacked BL TMDs due to the center-inversion symmetry and time-inversion symmetry.

(4) The electron energy dispersions in six types of high-symmetric BL TMDs are not parabolic like. The effective electron band mass and the fourth-order correction coefficient of the energy dispersion in different subbands depend strongly on the stacking configurations.

Although limited in scope, the results obtained from this study provide analytical insights lacking in the literature, and thereby help one gain an in-depth understanding of BL TMDs with different high-symmetric stacking structures. Moreover, our paper provides important input for subsequent transport and optical calculations, while opening further theoretical challenges using a similar approach. The predictions made in this paper are verifiable experimentally, and are relevant to any further use of bilayer TMDs in electronic and

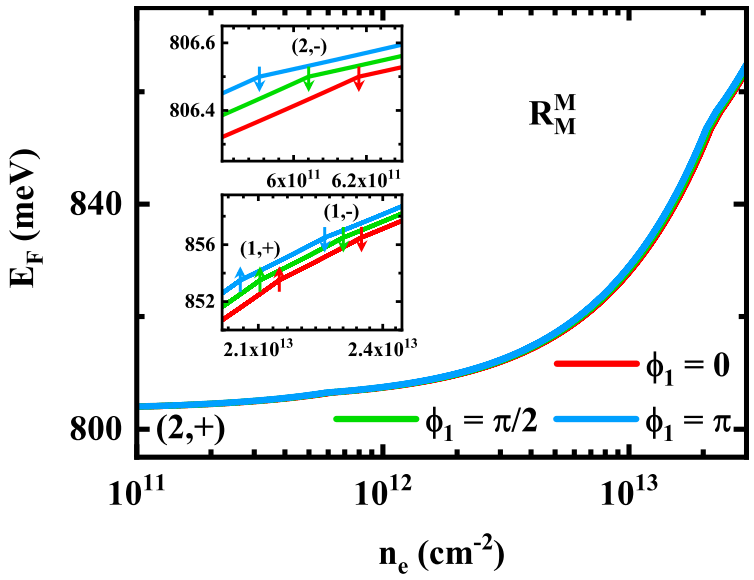

FIG. 12: The Fermi energy in R^M_M stacking BL MoS_2 for different ϕ_1 angles as indicated. Here (ν, γ) is the position of $E^{\gamma}_{c\nu}(0)$ and $\uparrow$ ($\downarrow$) denotes $\gamma = +$ $(-)$. The insets are the details of ϕ_1 dependence of E_F around $E^{-}_{c2}(0)$, $E^{+}_{c1}(0)$, and $E^{-}_{c1}(0)$.

optoelectronic devices, for which these materials are among the prominent vdW candidates.

ACKNOWLEDGMENTS

This work was supported by the National Natural Science foundation of China (NSFC) (Grants No. U2230122 and No. U2067207), Shenzhen Science and Technology Program (Grant No. KQTD20190929173954826), and by Research Foundation-Flanders (FWO).

APPENDIX

To understand the results presented and discussed in this work and for further application of these results in the calculation of electronic transport and optical properties of high-symmetric BL TMDs, here we present the coefficients regarding electron wavefunction in Eq. (4) and electron energy in Eq. (3) with specific stacking order. In these results, we define (μ, ν, τ, s, k) as the corresponding electron state with $E^{\gamma}_{\mu\nu}(k)$ and $\gamma = \tau s$.

A. H_M^M stacking order

For energy spectrum $E^{\gamma}_{\mu\nu}(k)$, we have

$$\begin{aligned}
b_3 =&0,\\
b_2 =&-2A^2k^2-\Delta^2/2-(\lambda_c^2+\lambda_v^2)-|t_{cc}|^2,\\
b_1 =&-\Delta(\lambda_c^2-\lambda_v^2)-\Delta|t_{cc}|^2,\\
b_0 =&A^4k^4+A^2k^2\Delta^2/2-2A^2k^2\lambda_c\lambda_v+\Delta^4/16\\
&-\Delta^2(\lambda_c^2+\lambda_v^2)/4+\lambda_c^2\lambda_v^2-(\Delta^2/4-\lambda_v^2)|t_{cc}|^2.
\end{aligned}\tag{A1}$$

For wavefunction at (μ,ν,τ,s,k) states with $E^{\gamma}_{\mu\nu}(k)$,

$$\begin{aligned}
c_1 =&-A^3k^2k_\tau^- t_{cc}+Ak_\tau^-(A^2k^2-h_c^-h_v^-)t_{cc},\\
c_2 =&A^2k_\tau^-k_\tau^-h_c^-t_{cc},\\
c_3 =&Ak_\tau^-(-A^2k^2+h_c^-h_v^-)h_c^-,\\
c_4 =&(A^2k^2-h_c^-h_v^-)h_c^+h_c^-+h_c^-h_v^-|t_{cc}|^2.
\end{aligned}\tag{A2}$$

B. H_X^M stacking order

For energy spectrum $E^{\gamma}_{\mu\nu}(k)$, we have

$$\begin{aligned}
b_3 =&0,\\
b_2 =&-2A^2k^2-\Delta^2/2-(\lambda_c^2+\lambda_v^2)-|t_{vv}|^2,\\
b_1 =&-\Delta(\lambda_c^2-\lambda_v^2)+\Delta|t_{vv}|^2,\\
b_0 =&A^4k^4+A^2k^2\Delta^2/2-2A^2k^2\lambda_c\lambda_v+\Delta^4/16\\
&-\Delta^2(\lambda_c^2+\lambda_v^2)/4+\lambda_c^2\lambda_v^2-(\Delta^2/4-\lambda_c^2)|t_{vv}|^2.
\end{aligned}\tag{B1}$$

For wavefunction at (μ,ν,τ,s,k) states with $E^{\gamma}_{\mu\nu}(k)$,

$$\begin{aligned}
c_1 =&-Ak_\tau^+h_c^+h_c^-t_{vv},\\
c_2 =&h_c^+h_c^-h_c^-t_{vv},\\
c_3 =&Ak_\tau^-(-A^2k^2+h_c^-h_v^-)h_c^-,\\
c_4 =&(A^2k^2-h_c^-h_v^-)h_c^+h_c^-.
\end{aligned}\tag{B2}$$

C. H_X^X stacking order

For energy spectrum $E^{\gamma}_{\mu\nu}(k)$, we have

$$\begin{aligned}
b_3 =&0,\\
b_2 =&-2A^2k^2-\Delta^2/2-(\lambda_c^2+\lambda_v^2)-|t_{cv}|^2-|t_{vc}|^2,\\
b_1 =&-\Delta(\lambda_c^2-\lambda_v^2)+\tau s(\lambda_c-\lambda_v)(|t_{cv}|^2-|t_{vc}|^2),\\
b_0 =&A^4k^4+A^2k^2\Delta^2/2-2A^2k^2\lambda_c\lambda_v\\
&-2A^2k^2|t_{cv}||t_{vc}|\cos\phi_2+\Delta^4/16\\
&-\Delta^2(\lambda_c^2+\lambda_v^2)/4+\lambda_c^2\lambda_v^2\\
&+\tau s\Delta(\lambda_c+\lambda_v)(|t_{cv}|^2-|t_{vc}|^2)/2\\
&+(\Delta^2/4+\lambda_c\lambda_v)(|t_{cv}|^2+|t_{vc}|^2)+|t_{cv}|^2|t_{vc}|^2.
\end{aligned}\tag{C1}$$

The H-stacked BL TMDs satisfy both center-inversion symmetry and time-reversal symmetry, which means τs disappears in Eq. (C1). Thus, $|t_{cv}| = |t_{vc}|$ (see the fourth line of b_0).

For wavefunction at (μ, ν, τ, s, k) states with $E^{\gamma}_{\mu\nu}(k)$,

$$\begin{aligned}
c_1 =&A^2k^2h_c^+t_{cv}+A^2k^2h_c^-t_{vc}-h_c^-t_{cv}|t_{vc}|^2-(A^2k^2-h_c^-h_v^-)h_c^+t_{cv},\\
c_2 =&-Ak_\tau^-h_c^+h_c^-t_{cv}-Ak_\tau^-h_c^-h_c^-t_{vc},\\
c_3 =&Ak_\tau^-(-A^2k^2+h_c^-h_v^-+t_{cv}t_{vc}^*)h_c^-,\\
c_4 =&(A^2k^2-h_c^-h_v^-)h_c^+h_c^-+h_c^-h_c^-|t_{vc}|^2.
\end{aligned}\tag{C2}$$

D. R_M^M stacking order

For energy spectrum $E^{\gamma}_{\mu\nu}(k)$, we have

$$\begin{aligned}
b_3 =& -2\tau s(\lambda_c+\lambda_v),\\
b_2 =& -2A^2k^2-\Delta^2/2-\tau s\Delta(\lambda_c-\lambda_v)+4\lambda_c\lambda_v+(\lambda_c^2+\lambda_v^2)-|t_{cc}|^2-|t_{vv}|^2,\\
b_1 =& 2A^2k^2\tau s(\lambda_c+\lambda_v)+\tau s\Delta^2(\lambda_c+\lambda_v)/2+\Delta(\lambda_c^2-\lambda_v^2)\\
&-2\tau s(\lambda_c^2\lambda_v+\lambda_c\lambda_v^2)-[\Delta-2\tau s\lambda_v]|t_{cc}|^2+[\Delta+2\tau s\lambda_c]|t_{vv}|^2,\\
b_0 =& A^4k^4+A^2k^2\Delta^2/2+A^2k^2\tau s\Delta(\lambda_c-\lambda_v)-2A^2k^2\lambda_c\lambda_v+\Delta^4/16\\
&-2A^2k^2|t_{cc}||t_{vv}|\cos\phi_1+\tau s\Delta^3(\lambda_c-\lambda_v)/4+\Delta^2(\lambda_c^2+\lambda_v^2)/4\\
&-\Delta^2\lambda_c\lambda_v-\tau s\Delta(\lambda_c^2\lambda_v-\lambda_c\lambda_v^2)+\lambda_c^2\lambda_v^2+\tau s\Delta(\lambda_v|t_{cc}|^2-\lambda_c|t_{vv}|^2)\\
&-(\Delta^2/4+\lambda_v^2)|t_{cc}|^2-(\Delta^2/4+\lambda_c^2)|t_{vv}|^2+|t_{cc}|^2|t_{vv}|^2.
\end{aligned}\tag{D1}$$

For wavefunction at (μ,ν,τ,s,k) states with $E^{\gamma}_{\mu\nu}(k)$,

$$\begin{aligned}
c_1 =& -A^3k^2k_\tau^- t_{cc}+Ak_\tau^-(A^2k^2-h_c^+h_v^+)t_{cc}-Ak_\tau^-h_c^+h_c^+t_{vv},\\
c_2 =& A^2k^2h_c^+t_{cc}+(h_c^+h_c^+-|t_{cc}|^2)h_c^+t_{vv},\\
c_3 =& Ak_\tau^-(-A^2k^2+h_c^+h_v^++t_{cc}^*t_{vv})h_c^+,\\
c_4 =& (A^2k^2-h_c^+h_v^+)h_c^+h_c^++h_c^+h_v^+|t_{cc}|^2.
\end{aligned}\tag{D2}$$

E. R_X^M stacking order

For energy spectrum $E^{\gamma}_{\mu\nu}(k)$, we have

$$\begin{aligned}
b_3 =& -2\tau s(\lambda_c+\lambda_v),\\
b_2 =& -2A^2k^2-\Delta^2/2-\tau s\Delta(\lambda_c-\lambda_v)+4\lambda_c\lambda_v+(\lambda_c^2+\lambda_v^2)-|t_{vc}|^2,\\
b_1 =& 2A^2k^2\tau s(\lambda_c+\lambda_v)+\tau s\Delta^2(\lambda_c+\lambda_v)/2+\Delta(\lambda_c^2-\lambda_v^2)\\
&-2\tau s(\lambda_c^2\lambda_v+\lambda_c\lambda_v^2)+\tau s(\lambda_c+\lambda_v)|t_{vc}|^2,\\
b_0 =& A^4k^4+A^2k^2\Delta^2/2+A^2k^2\tau s\Delta(\lambda_c-\lambda_v)-2A^2k^2\lambda_c\lambda_v\\
&+\Delta^4/16+\tau s\Delta^3(\lambda_c-\lambda_v)/4-\Delta^2\lambda_c\lambda_v+\Delta^2(\lambda_c^2+\lambda_v^2)/4\\
&-\tau s\Delta(\lambda_c^2\lambda_v-\lambda_c\lambda_v^2)+\lambda_c^2\lambda_v^2+\tau s\Delta(\lambda_c-\lambda_v)|t_{vc}|^2/2\\
&+(\Delta^2/4-\lambda_c\lambda_v)|t_{vc}|^2.
\end{aligned}\tag{E1}$$

For wavefunction at (μ,ν,τ,s,k) states with $E^{\gamma}_{\mu\nu}(k)$,

$$\begin{aligned}
c_1 =&A^2k_\tau^-k_\tau^-h_c^+t_{vc}-h_c^+t_{cv}|t_{vc}|^2,\\
c_2 =&-Ak_\tau^-h_c^+h_c^+t_{vc},\\
c_3 =&Ak_\tau^-(-A^2k^2+h_c^+h_v^+)h_c^+,\\
c_4 =&(A^2k^2-h_c^+h_v^+)h_c^+h_c^++h_c^+h_c^+|t_{vc}|^2.
\end{aligned}\tag{E2}$$

F. $\mathrm{R}^{\mathrm{X}}_{\mathrm{M}}$ stacking order

For energy spectrum $E^{\gamma}_{\mu\nu}(k)$, we have

$$\begin{aligned}
b_3 =&-2\tau s(\lambda_c+\lambda_v),\\
b_2 =&-2A^2k^2-\Delta^2/2-\tau s\Delta(\lambda_c-\lambda_v)+4\lambda_c\lambda_v+(\lambda_c^2+\lambda_v^2)-|t_{cv}|^2,\\
b_1 =&2A^2k^2\tau s(\lambda_c+\lambda_v)+\tau s\Delta^2(\lambda_c+\lambda_v)/2+\Delta(\lambda_c^2-\lambda_v^2)\\
&-2\tau s(\lambda_c^2\lambda_v+\lambda_c\lambda_v^2)+\tau s(\lambda_c+\lambda_v)|t_{cv}|^2,\\
b_0 =&A^4k^4+A^2k^2\Delta^2/2+A^2k^2\tau s\Delta(\lambda_c-\lambda_v)-2A^2k^2\lambda_c\lambda_v\\
&+\Delta^4/16+\tau s\Delta^3(\lambda_c-\lambda_v)/4-\Delta^2\lambda_c\lambda_v+\Delta^2(\lambda_c^2+\lambda_v^2)/4\\
&-\tau s\Delta(\lambda_c^2\lambda_v-\lambda_c\lambda_v^2)+\lambda_c^2\lambda_v^2+\tau s\Delta(\lambda_c-\lambda_v)|t_{cv}|^2/2\\
&+(\Delta^2/4-\lambda_c\lambda_v)|t_{cv}|^2.
\end{aligned}\tag{F1}$$

Through replacing $|t_{vc}|$ in Eq. (E1) with $|t_{cv}|$, we can get Eq. (F1). If $|t_{cv}|=|t_{vc}|$, the band energies of $\mathrm{R}^{\mathrm{M}}_{\mathrm{X}}$ and $\mathrm{R}^{\mathrm{X}}_{\mathrm{M}}$ are the same. As $\mathrm{R}^{\mathrm{M}}_{\mathrm{X}}$ is the result of operating out-of-plane mirror symmetry on $\mathrm{R}^{\mathrm{X}}_{\mathrm{M}}$, their band energies should be the same. Hence, $|t_{vc}|$ of $\mathrm{R}^{\mathrm{M}}_{\mathrm{X}}$ is equal to $|t_{cv}|$ of $\mathrm{R}^{\mathrm{X}}_{\mathrm{M}}$.

For wavefunction at (μ,ν,τ,s,k) states with $E^{\gamma}_{\mu\nu}(k)$,

$$\begin{aligned}
c_1 =&A^2k^2h_c^+t_{cv}-(A^2k^2-h_c^+h_v^+)h_c^+t_{cv},\\
c_2 =&-Ak_\tau^+h_c^+h_c^+t_{cv},\\
c_3 =&Ak_\tau^-(-A^2k^2+h_c^+h_v^+)h_c^+,\\
c_4 =&(A^2k^2-h_c^+h_v^+)h_c^+h_c^+.
\end{aligned}\tag{F2}$$

G. The allowed $t_{\mu\mu'}$ in six types of homo-BL TMDs

Following Refs. [6, 35], here we present the derivations to evaluate interlayer hopping matrix element given as $t_{\mu\mu'} = \langle \Psi^u_{\mu}(\mathbf{r})|H_{int}|\Psi^l_{\mu'}(\mathbf{r})\rangle$, where H_{int} is the interlayer hopping Hamiltonian between the two layers and is invariant under the C_3 rotation for six symmetric configurations of H and R staking. $\Psi^{u(l)}_{\tau\mu}(\mathbf{r})$ denotes the Bloch states at the K/K$'$ points and u (l) denote the upper (lower) layer, which are eigenstates of $\hat{C}_3$,

$$\begin{aligned}\hat{C}_3\Psi^u_{\tau\mu}(\mathbf{r}) &= e^{i\epsilon\tau\varphi^u}\gamma^u_m\Psi^u_{\tau\mu}(\mathbf{r}),\\ \hat{C}_3\Psi^l_{\tau\mu}(\mathbf{r}) &= e^{i\tau\varphi^l}\gamma^l_m\Psi^l_{\tau\mu}(\mathbf{r}),\end{aligned} \tag{G1}$$

where $\gamma_{m_{u(l)}} = e^{-i2m_{u(l)}\pi/3}$ is the eigenvalue of $\hat{C}_3$ operating on atomic orbits, $m_{u(l)} = 0$ for $\Psi^{u(l)}_{\tau c}(\mathbf{r})$, $m_u = 2\epsilon\tau$ for $\Psi^u_{\tau v}(\mathbf{r})$, and $m_l = 2\tau$ for $\Psi^l_{\tau v}(\mathbf{r})$. $\varphi^{u(l)}$ depends on rotation centers at M atom (M), X atom (X) or hollow center (h),

$$\varphi^{u(l)} = \begin{cases} 0, & \text{for M,}\\ \dfrac{2\pi}{3}, & \text{for X,}\\ -\dfrac{2\pi}{3}, & \text{for h.}\end{cases} \tag{G2}$$

Thus,

$$t_{\mu\mu'} = \langle \Psi^u_{\tau\mu}(\mathbf{r})|\hat{C}_3{}^{-1}\hat{C}_3 H_{int}\hat{C}_3{}^{-1}\hat{C}_3|\Psi^l_{\tau\mu'}(\mathbf{r})\rangle = \langle \hat{C}_3\Psi^u_{\tau\mu}(\mathbf{r})|H_{int}|\hat{C}_3\Psi^l_{\tau\mu'}(\mathbf{r})\rangle = e^{i\tau(\varphi^l-\epsilon\varphi^u)}\gamma^*_{m_u}\gamma_{m_l}t_{\mu\mu'}.$$

Consequently, $t_{\mu\mu'} \neq 0$ can only exist as $e^{i\tau(\varphi^l-\epsilon\varphi^u)}\gamma^*_{m_u}\gamma_{m_l} = 1$. For example, for $\mathrm{H}^{\mathrm{M}}_{\mathrm{X}}$ stacking ($\epsilon = -1$), its rotation center of upper (lower) layer is M (X), corresponding to $\varphi^u = 0$ and $\varphi^l = 2\pi/3$. Therefore, $e^{i\tau(\varphi^l-\epsilon\varphi^u)}\gamma^*_{m_u}\gamma_{m_l} = e^{-2\pi i\tau} = 1$ can only be satisfied by $\Psi^u_{\tau v}(\mathbf{r})$ and $\Psi^l_{\tau v}(\mathbf{r})$, namely only t_{vv} is allowed in this stacking order.

[1] K. S. Novoselov, A. K. Geim, S. V. Morozov, D. Jiang, Y. Zhang, S. V. Dubonos, I. V. Grigorieva, and A. A. Firsov, Electric field effect in atomically thin carbon films, Science **306**, 666-669 (2004).

[2] K. S. Novoselov, D. Jiang, F. Schedin, T. J. Booth, V. V. Khotkevich, S. V. Morozov, and A. K. Geim, Two-dimensional atomic crystals, Proc. Natl. Acad. Sci. U.S.A. **102**, 10451 (2005).

[3] C. Lee, Q. Li, W. Kalb, X.-Z. Liu, H. Berger, R. W. Carpick, and J. Hone, Frictional characteristics of atomically thin sheets, Science **328**, 76 (2010).

[4] F. V. Kusmartsev, W. M. Wu, M. P. Pierpoint, and K. C. Yung, in *Application of Graphene Within Optoelectronic Devices and Transistors*, Applied Spectroscopy and the Science of Nanomaterials (Springer, Singapore, 2015), pp. 191–221.

[5] D. Xiao, G.-B. Liu, W. Feng, X. Xu, and W. Yao, Coupled Spin and Valley Physics in Monolayers of MoS_2 and other group-VI Dichalcogenides, Phys. Rev. Lett. **108**, 196802 (2012).

[6] G.-B. Liu, D. Xiao, Y. Yao, X. Xu, and W. Yao, Electronic structures and theoretical modelling of two-dimensional group-VIB transition metal dichalcogenides, Chem. Soc. Rev. **44**, 2643 (2015).

[7] J. R. Schaibley, H. Yu, G. Clark, P. Rivera, J. S. Ross, K. L. Seyler, W. Yao, and X. Xu, Valleytronics in 2D materials, Nat. Rev. Mater. **1**, 16055 (2016).

[8] T. Habe and M. Koshino, Anomalous Hall effect in $2H$-phase MX_2 transition-metal dichalcogenide monolayers on ferromagnetic substrates (M = Mo, W, and X = S, Se, Te), Phys. Rev. B **96**, 085411 (2017).

[9] Z. Wu, B. T. Zhou, X. Cai, P. Cheung, G.-B. Liu, M. Huang, J. Lin, T. Han, L. An, Y. Wang, et al., Intrinsic valley Hall transport in atomically thin MoS_2, Nat. Commun. **10**, 611 (2019).

[10] S. Bhowal and S. Satpathy, Intrinsic orbital and spin Hall effects in monolayer transition metal dichalcogenides, Phys. Rev. B **102**, 035409 (2020).

[11] E. C. Ahn, 2D materials for spintronic devices, npj 2D Mater. Appl. **4**, 17 (2020).

[12] Y. Cao, V. Fatemi, S. Fang, K. Watanabe, T. Taniguchi, E. Kaxiras, and P. Jarillo-Herrero, Unconventional superconductivity in magic-angle graphene superlattices, Nature (London) **556**, 43 (2018).

[13] K. F. Mak and J. Shan, Semiconductor moiré materials, Nat. Nanotechnol. **17**, 686 (2022).

[14] A. Ciarrocchi, F. Tagarelli, A. Avsar, and A. Kis, Excitonic devices with van der Waals heterostructures: Valleytronics meets twistronics, Nat. Rev. Mater. **7**, 449 (2022).

[15] T. Jiang, H. Liu, D. Huang, S. Zhang, Y. Li, X. Gong, Y.-R. Shen, W.-T. Liu, and S. Wu, Valley and band structure engineering of folded MoS_2 bilayers, Nat. Nanotechnol. **9**, 825 (2014).

[16] M. Xia, B. Li, K. Yin, G. Capellini, G. Niu, Y. Gong, W. Zhou, P. M. Ajayan, and Y.-H. Xie, Spectroscopic Signatures of AA' and AB Stacking of chemical vapor deposited bilayer MoS_2,

ACS Nano **9**, 12246 (2015).

[17] A. K. Geim and I. V. Grigorieva, van der Waals heterostructures, Nature (London) **499**, 419 (2013).

[18] C. Q. Nguyen, Y. S. Ang, S.-T. Nguyen, N. V. Hoang, N. M. Hung, and C. V. Nguyen, Tunable type-II band alignment and electronic structure of $C_3N_4/MoSi_2N_4$ heterostructure: Interlayer coupling and electric field, Phys. Rev. B **105**, 045303 (2022).

[19] A. Kormányos, V. Zólyomi, V. I. Fal'ko, and G. Burkard, Tunable Berry curvature and valley and spin Hall effect in bilayer MoS_2, Phys. Rev. B **98**, 035408 (2018).

[20] J. Lee, K. F. Mak, and J. Shan, Electrical control of the valley Hall effect in bilayer MoS_2 transistors, Nat. Nanotechnol. **11**, 421 (2016).

[21] T. P. Cysne, M. Costa, L. M. Canonico, M. B. Nardelli, R. B. Muniz, and T. G. Rappoport, Disentangling orbital and valley Hall effects in bilayers of transition metal dichalcogenides, Phys. Rev. Lett. **126**, 056601 (2021).

[22] V. Vargiamidis, P. Vasilopoulos, M. Tahir, and N. Neophytou, Berry curvature, orbital magnetization, and Nernst effect in biased bilayer WSe_2, Phys. Rev. B **102**, 235426 (2020).

[23] Z. Gong, G.-B. Liu, H. Yu, D. Xiao, X. Cui, X. Xu, and W. Yao, Magnetoelectric effects and valley-controlled spin quantum gates in transition metal dichalcogenide bilayers, Nat. Commun. **4**, 2053 (2013).

[24] A. M. Jones, H. Yu, J. S. Ross, P. Klement, N. J. Ghimire, J. Yan, D. G. Mandrus, W. Yao, and X. Xu, Spin–layer locking effects in optical orientation of exciton spin in bilayer WSe_2, Nat. Phys. **10**, 130 (2014).

[25] A. Castellanos-Gomez, X. Duan, Z. Fei, H. R. Gutierrez, Y. Huang, X. Huang, J. Quereda, Q. Qian, E. Sutter, and P. W. Sutter, van der Waals heterostructures, Nat. Rev. Methods **2**, 58 (2022).

[26] J. Shi, P. Yu, F. Liu, P. He, R. Wang, L. Qin, J. Zhou, X. Li, J. Zhou, X. Sui, et al., 3R MoS_2 with broken inversion symmetry: A promising ultrathin nonlinear optical device, Adv. Mater. **29**, 1701486 (2017).

[27] S. Shree, D. Lagarde, L. Lombez, C. Robert, A. Balocchi, K. Watanabe, T. Taniguchi, X. Marie, I. C. Gerber, M. M. Glazov, et al., Interlayer exciton mediated second harmonic generation in bilayer MoS_2, Nat. Commun. **12**, 6894 (2021).

[28] I. C. Gerber, E. Courtade, S. Shree, C. Robert, T. Taniguchi, K. Watanabe, A. Balocchi, P.

Renucci, D. Lagarde, X. Marie, and B. Urbaszek, Interlayer excitons in bilayer MoS_2 with strong oscillator strength up to room temperature, Phys. Rev. B **99**, 035443 (2019).

[29] G.-B. Liu, W.-Y. Shan, Y. Yao, W. Yao, and D. Xiao, Three-band tight-binding model for monolayers of group-VIB transition metal dichalcogenides, Phys. Rev. B **88**, 085433 (2013).

[30] K. V. Shanavas and S. Satpathy, Effective tight-binding model for MX_2 under electric and magnetic fields, Phys. Rev. B **91**, 235145 (2015).

[31] M. El-Batanouny, *Advanced Quantum Condensed Matter Physics: One-Body, Many-Body, and Topological Perspectives* (Cambridge University, Cambridge, 2020).

[32] Q. Tong, H. Yu, Q. Zhu, Y. Wang, X. Xu, and W. Yao, Topological mosaics in moiré superlattices of van der Waals heterobilayers, Nat. Phys. **13**, 356 (2017).

[33] M. Tahir, P. M. Krstajić, and P. Vasilopoulos, Electrically controlled dc and ac transport in bilayer WSe_2, Phys. Rev. B **98**, 075429 (2018).

[34] M. Zubair, M. Tahir, and P. Vasilopoulos, Magneto-optical properties of bilayer transition metal dichalcogenides, Phys. Rev. B **98**, 155402 (2018).

[35] See Supplemental Material of Ref. [32].

[36] Y. Wang, Z. Wang, W. Yao, G.-B. Liu, and H. Yu, Interlayer coupling in commensurate and incommensurate bilayer structures of transition-metal dichalcogenides, Phys. Rev. B **95**, 115429 (2017).

[37] J. M. Lu, O. Zheliuk, I. Leermakers, N. F. Q. Yuan, U. Zeitler, K. T. Law, and J. T. Ye, Evidence for two-dimensional Ising superconductivity in gated MoS_2, Science **350**, 1353 (2015).

[38] H. Rostami, K. Volckaert, N. Lanata, S. K. Mahatha, C. E. Sanders, M. Bianchi, D. Lizzit, L. Bignardi, S. Lizzit, J. A. Miwa, A. V. Balatsky, P. Hofmann, and S. Ulstrup, Layer and orbital interference effects in photoemission from transition metal dichalcogenides, Phys. Rev. B **100**, 235423 (2019).

[39] X. N. Zhao, W. Xu, Y. M. Xiao, J. Liu, B. Van Duppen, and F. M. Peeters, Terahertz optical Hall effect in monolayer MoS_2 in the presence of proximity-induced interactions, Phys. Rev. B **101**, 245412 (2020).

[40] F. W. Han, W. Xu, L. L. Li, C. Zhang, H. M. Dong, and F. M. Peeters, Electronic and transport properties of n-type monolayer black phosphorus at low temperatures, Phys. Rev. B **95**, 115436 (2017).

[41] K. Kośmider, J. W. González, and J. Fernández-Rossier, Large spin splitting in the conduction

band of transition metal dichalcogenide monolayers, Phys. Rev. B **88**, 245436 (2013).

[42] W. Xu, Electron density of states in terahertz driven two-dimensional electron gases, Semicond. Sci. Technol. **12**, 1559 (1997).